Centrality and transverse momentum dependence of D^0-meson production at mid-rapidity in Au+Au collisions at $\sqrt{s_{\mathrm{NN}}} = 200\,\mathrm{GeV}$

J. Adam[12], L. Adamczyk[2], J. R. Adams[34], J. K. Adkins[25], G. Agakishiev[23], M. M. Aggarwal[36], Z. Ahammed[56],
I. Alekseev[3,30], D. M. Anderson[50], R. Aoyama[53], A. Aparin[23], D. Arkhipkin[5], E. C. Aschenauer[5], M. U. Ashraf[52],
F. Atetalla[24], A. Attri[36], G. S. Averichev[23], V. Bairathi[31], K. Barish[9], A. J. Bassill[9], A. Behera[48],
R. Bellwied[19], A. Bhasin[22], A. K. Bhati[36], J. Bielcik[13], J. Bielcikova[33], L. C. Bland[5], I. G. Bordyuzhin[3],
J. D. Brandenburg[5], A. V. Brandin[30], D. Brown[27], J. Bryslawskyj[9], I. Bunzarov[23], J. Butterworth[41], H. Caines[59],
M. Calderón de la Barca Sánchez[7], D. Cebra[7], I. Chakaberia[24,45], P. Chaloupka[13], B. K. Chan[8], F-H. Chang[32],
Z. Chang[5], N. Chankova-Bunzarova[23], A. Chatterjee[56], S. Chattopadhyay[56], J. H. Chen[46], X. Chen[44], J. Cheng[52],
M. Cherney[12], W. Christie[5], G. Contin[26], H. J. Crawford[6], M. Csanad[15], S. Das[10], T. G. Dedovich[23],
I. M. Deppner[18], A. A. Derevschikov[38], L. Didenko[5], C. Dilks[37], X. Dong[26], J. L. Drachenberg[1], J. C. Dunlop[5],
T. Edmonds[39], L. G. Efimov[23], N. Elsey[58], J. Engelage[6], G. Eppley[41], R. Esha[8], S. Esumi[53], O. Evdokimov[11],
J. Ewigleben[27], O. Eyser[5], R. Fatemi[25], S. Fazio[5], P. Federic[33], J. Fedorisin[23], P. Filip[23], E. Finch[47], Y. Fisyak[5],
C. E. Flores[7], L. Fulek[2], C. A. Gagliardi[50], T. Galatyuk[14], F. Geurts[41], A. Gibson[55], L. Greiner[26], D. Grosnick[55],
D. S. Gunarathne[49], Y. Guo[24], A. Gupta[22], W. Guryn[5], A. I. Hamad[24], A. Hamed[50], A. Harlenderova[13],
J. W. Harris[59], L. He[39], S. Heppelmann[7], S. Heppelmann[37], N. Herrmann[18], A. Hirsch[39], L. Holub[13], Y. Hong[26],
S. Horvat[59], B. Huang[11], H. Z. Huang[8], S. L. Huang[48], T. Huang[32], X. Huang[52], T. J. Humanic[34], P. Huo[48],
G. Igo[8], W. W. Jacobs[20], A. Jentsch[51], J. Jia[5,48], K. Jiang[44], S. Jowzaee[58], X. Ju[44], E. G. Judd[6], S. Kabana[24],
S. Kagamaster[27], D. Kalinkin[20], K. Kang[52], D. Kapukchyan[9], K. Kauder[5], H. W. Ke[5], D. Keane[24],
A. Kechechyan[23], M. Kelsey[26], D. P. Kikoła[57], C. Kim[9], T. A. Kinghorn[7], I. Kisel[16], A. Kisiel[57], M. Kocan[13],
L. Kochenda[30], L. K. Kosarzewski[13], A. F. Kraishan[49], L. Kramarik[13], L. Krauth[9], P. Kravtsov[30], K. Krueger[4],
N. Kulathunga Mudiyanselage[19], L. Kumar[36], R. Kunnawalkam Elayavalli[58], J. Kvapil[13], J. H. Kwasizur[20],
R. Lacey[48], J. M. Landgraf[5], J. Lauret[5], A. Lebedev[5], R. Lednicky[23], J. H. Lee[5], C. Li[44], W. Li[46], W. Li[41], X. Li[44],
Y. Li[52], Y. Liang[24], R. Licenik[13], J. Lidrych[13], T. Lin[50], A. Lipiec[57], M. A. Lisa[34], F. Liu[10], H. Liu[20], P. Liu[48],
P. Liu[46], X. Liu[34], Y. Liu[50], Z. Liu[44], T. Ljubicic[5], W. J. Llope[58], M. Lomnitz[26], R. S. Longacre[5], S. Luo[11],
X. Luo[10], G. L. Ma[46], L. Ma[17], R. Ma[5], Y. G. Ma[46], N. Magdy[11], R. Majka[59], D. Mallick[31], S. Margetis[24],
C. Markert[51], H. S. Matis[26], O. Matonoha[13], J. A. Mazer[42], K. Meehan[7], J. C. Mei[45], N. G. Minaev[38],
S. Mioduszewski[50], D. Mishra[31], B. Mohanty[31], M. M. Mondal[21], I. Mooney[58], Z. Moravcova[13], D. A. Morozov[38],
M. Mustafa[26], Md. Nasim[8], K. Nayak[10], J. M. Nelson[6], D. B. Nemes[59], M. Nie[46], G. Nigmatkulov[30], T. Niida[58],
L. V. Nogach[38], T. Nonaka[10], G. Odyniec[26], A. Ogawa[5], K. Oh[40], S. Oh[59], V. A. Okorokov[30], D. Olvitt Jr.[49],
B. S. Page[5], R. Pak[5], Y. Panebratsev[23], B. Pawlik[35], H. Pei[10], C. Perkins[6], R. L. Pinter[15], J. Pluta[57], J. Porter[26],
M. Posik[49], N. K. Pruthi[36], M. Przybycien[2], J. Putschke[58], A. Quintero[49], H. Qiu[26], S. K. Radhakrishnan[26],
R. L. Ray[51], R. Reed[27], H. G. Ritter[26], J. B. Roberts[41], O. V. Rogachevskiy[23], J. L. Romero[7], L. Ruan[5],
J. Rusnak[33], O. Rusnakova[13], N. R. Sahoo[50], P. K. Sahu[21], S. Salur[42], J. Sandweiss[59], J. Schambach[51],
A. M. Schmah[26], W. B. Schmidke[5], N. Schmitz[28], B. R. Schweid[48], F. Seck[14], J. Seger[12], M. Sergeeva[8], R. Seto[9],
P. Seyboth[28], N. Shah[46], E. Shahaliev[23], P. V. Shanmuganathan[27], M. Shao[44], F. Shen[45], W. Q. Shen[46], S. S. Shi[10],
Q. Y. Shou[46], E. P. Sichtermann[26], S. Siejka[57], R. Sikora[2], M. Simko[33], JSingh[36], S. Singha[24], D. Smirnov[5],
N. Smirnov[59], W. Solyst[20], P. Sorensen[5], H. M. Spinka[4], B. Srivastava[39], T. D. S. Stanislaus[55], D. J. Stewart[59],
M. Strikhanov[30], B. Stringfellow[39], A. A. P. Suaide[43], T. Sugiura[53], M. Sumbera[33], B. Summa[37], X. M. Sun[10],
Y. Sun[44], B. Surrow[49], D. N. Svirida[3], M. Szelezniak[26], P. Szymanski[57], A. H. Tang[5], Z. Tang[44], A. Taranenko[30],
T. Tarnowsky[29], J. H. Thomas[26], A. R. Timmins[19], T. Todoroki[5], M. Tokarev[23], C. A. Tomkiel[27], S. Trentalange[8],
R. E. Tribble[50], P. Tribedy[5], S. K. Tripathy[21], O. D. Tsai[8], B. Tu[10], T. Ullrich[5], D. G. Underwood[4], I. Upsal[5,45],
G. Van Buren[5], J. Vanek[33], A. N. Vasiliev[38], I. Vassiliev[16], F. Videbæk[5], S. Vokal[23], S. A. Voloshin[58], A. Vossen[20],
F. Wang[39], G. Wang[8], P. Wang[44], Y. Wang[10], Y. Wang[52], J. C. Webb[5], L. Wen[8], G. D. Westfall[29], H. Wieman[26],
S. W. Wissink[20], R. Witt[54], Y. Wu[24], Z. G. Xiao[52], G. Xie[11], W. Xie[39], N. Xu[26], Q. H. Xu[45], Y. F. Xu[46],
Z. Xu[5], C. Yang[45], Q. Yang[45], S. Yang[5], Y. Yang[32], Z. Ye[41], Z. Ye[11], L. Yi[45], K. Yip[5], I. -K. Yoo[40],
H. Zbroszczyk[57], W. Zha[44], D. Zhang[10], J. Zhang[48], L. Zhang[10], S. Zhang[44], S. Zhang[46], X. P. Zhang[52],
Y. Zhang[44], Z. Zhang[46], J. Zhao[39], C. Zhong[46], C. Zhou[46], X. Zhu[52], Z. Zhu[45], M. K. Zurek[26], M. Zyzak[16]

[1]*Abilene Christian University, Abilene, Texas 79699*
[2]*AGH University of Science and Technology, FPACS, Cracow 30-059, Poland*
[3]*Alikhanov Institute for Theoretical and Experimental Physics, Moscow 117218, Russia*
[4]*Argonne National Laboratory, Argonne, Illinois 60439*
[5]*Brookhaven National Laboratory, Upton, New York 11973*

^{6}University of California, Berkeley, California 94720

^{7}University of California, Davis, California 95616

^{8}University of California, Los Angeles, California 90095

^{9}University of California, Riverside, California 92521

^{10}Central China Normal University, Wuhan, Hubei 430079

^{11}University of Illinois at Chicago, Chicago, Illinois 60607

^{12}Creighton University, Omaha, Nebraska 68178

^{13}Czech Technical University in Prague, FNSPE, Prague 115 19, Czech Republic

^{14}Technische Universität Darmstadt, Darmstadt 64289, Germany

^{15}Eötvös Loránd University, Budapest, Hungary H-1117

^{16}Frankfurt Institute for Advanced Studies FIAS, Frankfurt 60438, Germany

^{17}Fudan University, Shanghai, 200433

^{18}University of Heidelberg, Heidelberg 69120, Germany

^{19}University of Houston, Houston, Texas 77204

^{20}Indiana University, Bloomington, Indiana 47408

^{21}Institute of Physics, Bhubaneswar 751005, India

^{22}University of Jammu, Jammu 180001, India

^{23}Joint Institute for Nuclear Research, Dubna 141 980, Russia

^{24}Kent State University, Kent, Ohio 44242

^{25}University of Kentucky, Lexington, Kentucky 40506-0055

^{26}Lawrence Berkeley National Laboratory, Berkeley, California 94720

^{27}Lehigh University, Bethlehem, Pennsylvania 18015

^{28}Max-Planck-Institut für Physik, Munich 80805, Germany

^{29}Michigan State University, East Lansing, Michigan 48824

^{30}National Research Nuclear University MEPhI, Moscow 115409, Russia

^{31}National Institute of Science Education and Research, HBNI, Jatni 752050, India

^{32}National Cheng Kung University, Tainan 70101

^{33}Nuclear Physics Institute of the CAS, Rez 250 68, Czech Republic

^{34}Ohio State University, Columbus, Ohio 43210

^{35}Institute of Nuclear Physics PAN, Cracow 31-342, Poland

^{36}Panjab University, Chandigarh 160014, India

^{37}Pennsylvania State University, University Park, Pennsylvania 16802

^{38}Institute of High Energy Physics, Protvino 142281, Russia

^{39}Purdue University, West Lafayette, Indiana 47907

^{40}Pusan National University, Pusan 46241, Korea

^{41}Rice University, Houston, Texas 77251

^{42}Rutgers University, Piscataway, New Jersey 08854

^{43}Universidade de São Paulo, São Paulo, Brazil 05314-970

^{44}University of Science and Technology of China, Hefei, Anhui 230026

^{45}Shandong University, Qingdao, Shandong 266237

^{46}Shanghai Institute of Applied Physics, Chinese Academy of Sciences, Shanghai 201800

^{47}Southern Connecticut State University, New Haven, Connecticut 06515

^{48}State University of New York, Stony Brook, New York 11794

^{49}Temple University, Philadelphia, Pennsylvania 19122

^{50}Texas A&M University, College Station, Texas 77843

^{51}University of Texas, Austin, Texas 78712

^{52}Tsinghua University, Beijing 100084

^{53}University of Tsukuba, Tsukuba, Ibaraki 305-8571, Japan

^{54}United States Naval Academy, Annapolis, Maryland 21402

^{55}Valparaiso University, Valparaiso, Indiana 46383

^{56}Variable Energy Cyclotron Centre, Kolkata 700064, India

^{57}Warsaw University of Technology, Warsaw 00-661, Poland

^{58}Wayne State University, Detroit, Michigan 48201 and

^{59}Yale University, New Haven, Connecticut 06520

(STAR Collaboration)

(Dated: December 5, 2018)

We report a new measurement of D^0-meson production at mid-rapidity ($|y| < 1$) in Au+Au collisions at $\sqrt{s_{NN}} = 200\,\mathrm{GeV}$ utilizing the Heavy Flavor Tracker, a high resolution silicon detector at the STAR experiment. Invariant yields of D^0-mesons in the transverse momenta (p_T) < 9 GeV/c is reported in various centrality bins (0-10%, 10-20%, 20-40%, 40-60% and 60-80%). Blast-Wave thermal models are fit to D^0-meson p_T spectra to study D^0 hadron kinetic freeze-out temperature and radial flow velocity. The average radial flow velocity extracted from the fit is considerably smaller compared to that of light hadrons (π, K, p), but comparable to that of hadrons containing

multiple strange quarks (ϕ, Ξ^-), indicating D^0 mesons kinetically decouple from the system earlier than light hadrons. The calculated D^0 nuclear modification factors re-affirm that charm quarks suffer large amount of energy loss in the hot QCD similar to those of light quarks for $p_T > 4\,\mathrm{GeV}/c$ in central 0-10% Au+Au collisions. For low p_T, the nuclear modification factor shows a characteristic structure consistent with the expectation from model predictions that charm quarks gain sizable collective motion during the medium evolution. The new improved measurements are expected to further constrain parameters and reduce their uncertainties in model calculations.

I. INTRODUCTION

The heavy ion program at the Relativistic Heavy Ion Collider (RHIC) and Large Hadron Collider (LHC) mainly studies Quantum Chromodynamics (QCD) at high temperature and density. Over the last few papers, experimental results from RHIC and LHC using light flavor probes have demonstrated that a strongly-coupled Quark-Gluon Plasma (sQGP) is created in these heavy-ion collisions. The most significant evidence comes from the strong collective flow and the large high transverse momentum (p_T) suppression in central collisions for various observed hadrons including multi-strange-quark hadrons ϕ and Ω [1–5].

Heavy quarks (c,b) are created predominantly through initial hard scatterings due to their large masses [6, 7]. The modification to their production in transverse momentum due to energy loss and radial flow and in azimuth due to anisotropic flows is sensitive to heavy quark dynamics in the partonic sQGP phase [8]. Recent measurements of high-p_T D-meson production at RHIC and LHC show a strong suppression in the central heavy-ion collisions. The nuclear modification factor R_{AA}:

$$R_{\mathrm{AA}} = \frac{1}{<N_{\mathrm{bin}}>} \frac{d^2 N_{\mathrm{AA}}/dp_T}{d^2 N_{pp}/dp_T}. \qquad (1)$$

which is the ratio between the yield in heavy-ion collisions and the average number-of-binary-collisions scaled yield in $p+p$ collisions, is used to quantify its level [9–12]. The D meson suppression is similar to that of light hadrons at $p_T > 4\,\mathrm{GeV}/c$, suggesting significant energy loss for charm quarks inside the sQGP medium. The measured D-meson anisotropic flow shows that D-mesons also exhibit significant elliptic and triangular flow at RHIC and LHC [13–16]. The magnitude when scaled with the transverse kinetic energy is similar to that of light and strange flavor hadrons. This indicates that charm quarks may behave like they reached thermal equilibrium in these collisions at RHIC and LHC.

In this article, we report measurements of the centrality dependence of D^0-meson transverse momentum spectra at mid-rapidity ($|y| < 1$) in Au+Au collisions at $\sqrt{s_{\mathrm{NN}}} = 200\,\mathrm{GeV}$. The measurements are conducted at the Solenoidal Tracker At RHIC (STAR) experiment utilizing the high resolution silicon detector (the Heavy Flavor Tracker, HFT) [17]. The paper is organized in the following order: In Sec. II, we describe the detector setup and dataset used in this analysis. In Sec. III, we present the topological reconstruction of D^0 mesons in the Au+Au collision data, followed by Sec. IV and Sec. V for details on efficiency corrections and systematic uncertainties. We present our measurement results and physics discussions in Sec. VI. Finally, we end the paper with a summary in Sec. VII .

II. EXPERIMENTAL SETUP AND DATASET

The dataset used in this analysis consists of Au+Au collision events at $\sqrt{s_{\mathrm{NN}}} = 200\,\mathrm{GeV}$ collected by the Solenoid Tracker detector At RHIC (STAR) in the 2014 year run. The main detectors used in this analysis are the Time Projection Chamber (TPC), the Heavy Flavor Tracker detector, the Time of Flight (TOF) detector and the Vertex Position Detector (VPD).

A. Tracking Devices

Precision tracking for this analysis is achieved with TPC and HFT detectors and particle identification for stable hadrons are performed with a combination of the ionization energy loss (dE/dx) measurement with the TPC and the time-of-flight (tof) measurement with TOF detector. The event start time is provided by the VPD. Both TPC and TOF detectors have full azimuthal coverage with a pseudo rapidity range of $|\eta| < 1$ [18, 19]. Both TPC and TOF have been extensively used in many prior STAR measurements [4, 12, 20]. The HFT detector provides high-pointing resolution to the vicinity of the event vertex by providing high precision points that are used to extend track trajectories.

B. Trigger

The minimum bias trigger used in this analysis is defined as a coincidence between the east and west VPD detectors located at $4.4 < |\eta| < 4.9$ [21]. Each VPD detector is an assembly of nineteen small detectors, each consisting of a Pb converter followed by a fast, plastic scintillator read out by a photomultiplier tube. To efficiently sample the collision events in the center of HFT acceptance, an online cut of collision vertex along the beam line (calculated via the time difference between east and west VPD detectors) $|V_z^{\mathrm{VPD}}| < 6$ cm is applied. The decrease in the coincidence probability in VPD degrades the online VPD vertex resolution in peripheral low multiplicity events. These inefficiencies are corrected with the methods discussed in the next section.

C. Trigger Efficiency and Centrality Selection

Events used in this analysis are selected with the reconstructed collision vertex (Primary Vertex, V_z^{TPC}) within 6 cm of the TPC and HFT centers along the beam direction to ensure uniform and large acceptance. The maximum total drift time of ionization electrons inside the TPC is about $40\,\mu s$ while the hadronic Au+Au collision rate is typically around $40\,\mathrm{kHz}$ during when this dataset was recorded. There is a finite chance that more than one event is recorded in the TPC readout event frame. The VPD is a fast detector which can separate events from different bunch crossings (one bunch cross at RHIC is 106 ns). In order to suppress the chance of selecting the wrong vertex from collisions in bunch crossings different from that of the trigger, the difference between the event vertex z coordinate V_z^{TPC} and the V_z^{VPD} is required to be less than 3 cm. Approximately 9×10^8 minimum bias triggered events with 0-80% centrality passed the selection criteria and are used in this analysis.

The centrality is selected using the measured charged global track multiplicity $N_{\mathrm{ch}}^{\mathrm{raw}}$ at midrapidity within $|\eta| < 0.5$ and corrected for the online VPD triggering inefficiency using a Monte Carlo (MC) Glauber simulation. 0-X% centrality is defined as the 0-X% most central in terms of total hadronic cross section determined by the impact parameter between two colliding nuclei. In this analysis, the dependence of $N_{\mathrm{ch}}^{\mathrm{raw}}$ on the collision vertex position and the beam luminosity has been taken into account. The measured track multiplicity distribution from Au+Au $200\,\mathrm{GeV}$ from RHIC run 2014, corrected for the vertex and luminosity dependence, is shown in Fig. 1. The measured distribution is fit to the MC Glauber calculation in the high multiplicity region. One can observe that the fitted MC Glauber calculation matches the real data well for $N_{\mathrm{ch}}^{\mathrm{raw}} > 100$, while the discrepancy in the low multiplicity region shows the VPD trigger inefficiency. Figure 1 panel (b) shows the ratio between MC and data. Centrality is defined according to the MC Glauber model distribution shown in panel (a). Events in the low-multiplicity region are weighted with the ratio shown in panel (b) in all the following analysis as a correction for the inefficiency in trigger. The very high end discrepancy is due to the fitting precision while it has very tiny contribution.

Table I lists the extracted values of number of binary collisions (N_{bin}), number of participants (N_{part}) and trigger inefficiency correction factors ($\varepsilon_{\mathrm{trg}}$) as well as their uncertainties. The $\varepsilon_{\mathrm{trg}}$ factors are the average values over in each centrality bins. In practice we apply this correction factor event-by-event according to the measured $N_{\mathrm{ch}}^{\mathrm{raw}}$ for each event.

D. Heavy Flavor Tracker

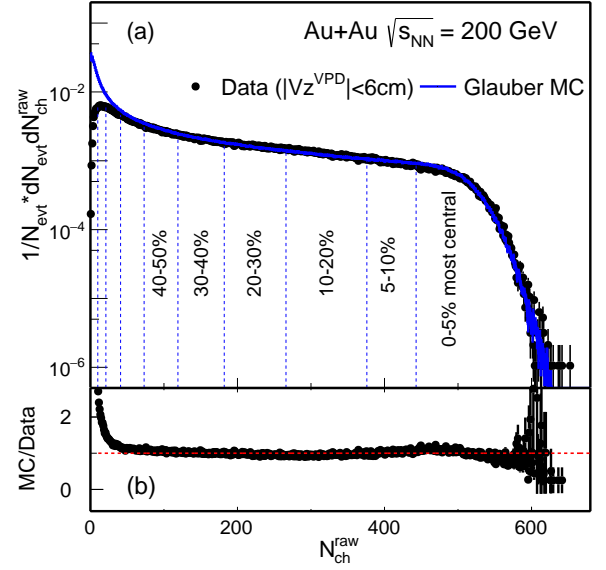The HFT [17] is a high resolution silicon detector system, that aims for the topological reconstruction of sec-

FIG. 1. (a) Uncorrected charged particle multiplicity $N_{\mathrm{ch}}^{\mathrm{raw}}$ distribution measured with $|\eta| < 0.5$ and $|Vz^{\mathrm{TPC}}| < 6$ cm. The solid curve depicts the multiplicity distribution from a MC Glauber simulation fit to the experimental data. (b) Ratio between MC simulation and real data

ondary decay vertices. It consists of three silicon subsystems: the Silicon Strip Detector (SSD), the Intermediate Silicon Tracker (IST), and two layers of the PiXeL (PXL) detector. Table II lists the key characteristic parameters of each subsystem. The SSD detector was still under commission stage during when the dataset was recorded, and therefore is not used in the offline data production and this analysis. The PXL detector uses the new Monolithic Active Pixel Sensors (MAPS) technology [22]. This is the first application of this technology in a collider experiment. It is particularly designed to measure heavy-flavor hadron decays in the high multiplicity heavy-ion collision environment.

In the offline reconstruction, tracks are reconstructed in the TPC first and then extended to the HFT detector to find the best fit to the measured high resolution spatial points. The tracking algorithm with the Kalman filter that considers various detector material effects is used in the track extension. Considering the background hits level in the PXL due to pileup hadronic and electromagnetic collisions, tracks are required to have at least one hit in each layer of the IST and PXL subdetectors. Figure 2 shows the track pointing resolution to the primary vertex in the transverse plane (σ_{XY}) in panel (a) and along the longitudinal direction (σ_{Z}) in panel (b) as a function of momentum (p) for identified particles in $0-80\%$ centrality Au+Au collisions. The design goal for the HFT detector was to have a pointing resolution better than $55\,\mu m$ for $750\,\mathrm{MeV}$ Kaons. Figure 2 demonstrates that the HFT detector system meets the design requirements. This performance enabled the study of the D-meson production with a high significance signal.
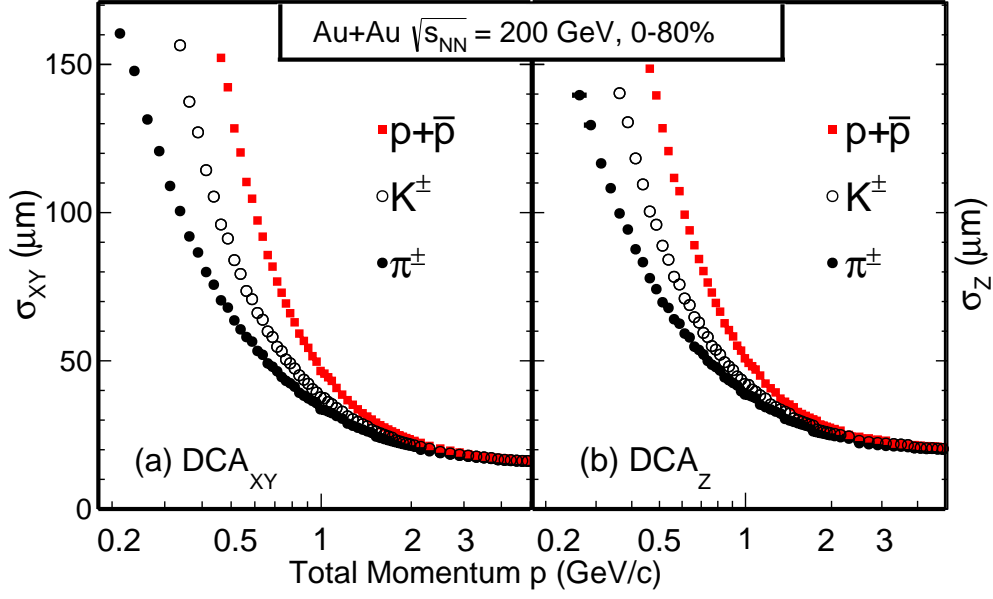
FIG. 2. Identified particle ($\pi^{\pm}$, $K^{\pm}$, and $p+\bar{p}$) pointing resolution in the transverse (a) and longitudinal (b) planes as a function of particle total momentum in Au+Au 0–80% collisions.

TABLE I. Estimated values of number of binary collisions (N_{bin}), number of participants (N_{part}) and trigger correction factors ($\varepsilon_{\mathrm{trg}}$, uncertainties negligible) for various centrality bins obtained from the MC Glauber model fit to the measured multiplicity distributions.

Centrality	N_{bin}	N_{part}	$\varepsilon_{\mathrm{trg}}$
0–10 %	938.8 $\pm$ 26.3	319.4 $\pm$ 3.4	1.0
10–20 %	579.9 $\pm$ 28.8	227.6 $\pm$ 7.9	1.0
20–40 %	288.3 $\pm$ 30.4	137.6 $\pm$ 10.4	1.0
40–60 %	91.3 $\pm$ 21.0	60.5 $\pm$ 10.1	0.92
60–80 %	21.3 $\pm$ 8.9	20.4 $\pm$ 6.6	0.65

III. D^0-MESON RECONSTRUCTION

D^0 and $\overline{D}^0$ mesons are reconstructed via the hadronic decay channel $D^0 \to K^- + \pi^+$ and its charge conjugate channel with a branching ratio of 3.89%. In what follows, we imply $(D^0 + \overline{D}^0)/2$ when using the term D^0 unless otherwise specified. D^0 mesons decay with a proper decay length of $c\tau \sim 123$ μm after they are produced in Au+Au collisions. We utilize the high-pointing resolution capability enabled by the HFT detector to topologically reconstruct the D^0 decay vertices that are separated from the collision vertices, which drastically reduces ($\sim$5 order of magnitude) the combinational background and improves the measurement precision.

Charged pion and kaon tracks are reconstructed with the TPC and the HFT. Tracks are required to have at least 20 measured TPC points out of maximum 45 to ensure with good momentum resolution. To enable high pointing precision, both daughter tracks are required to have at least one measured hit in each layer of PXL and

IST as described above. Particle identification is achieved via a combination of the ionization energy loss measurement in the TPC and the tof measurement in the TOF. The resolution-normalized dE/dx deviation from the expected values is defined as:

$$n\sigma_X = \frac{1}{R} \ln \frac{\langle dE/dx \rangle_{mea.}}{\langle dE/dx \rangle_X}, \qquad (2)$$

where $\langle dE/dx \rangle_{mea.}$ and $\langle dE/dx \rangle_X$ represent measured and expected dE/dx, and R is the STAR TPC dE/dx resolution (typically $\sim$8% [18]). The $n\sigma_X$ should be close to a standard Gaussian distribution for each corresponding particle species (mean = 0, $\sigma = 1$). Pion (kaon) candidates are selected by a requirement of the measured dE/dx to be within three (two) standard deviations ($|n\sigma_X|$) from the expected value. When tracks have matched hits in the TOF detector, an additional requirement on the measured inverse particle velocity ($1/\beta$) to be within three standard deviations from the expected value ($|\Delta 1/\beta|$) is applied for either daughter track. Fig-

TABLE II. Several key characteristic parameters for each subsystem of the HFT detector.

Subsystem	Radius (cm)	Length (cm)	Thickness at $\eta = 0$ (X_0)	Pitch Size (μm^2)
PXL inner layer	2.8	20	0.52% (0.39%[†])	20.7×20.7
PXL outer layer	8.0	20	0.52%	20.7×20.7
IST	14.0	50	1.0%	600×6000
SSD[††]	22.0	106	1.0%	95×40000

[†] - PXL inner detector material is reduced to $0.39\% X_0$ in 2015/2016 runs.
[††] - SSD is not included in this analysis.
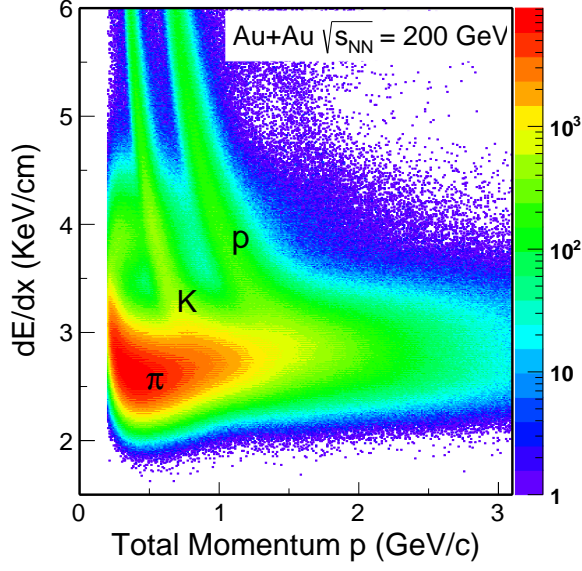
FIG. 3. TPC dE/dx vs. particle momentum.
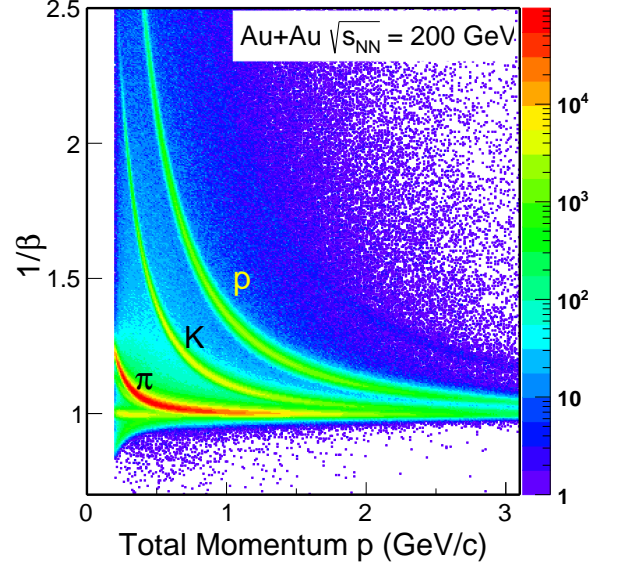
FIG. 4. TOF $1/\beta$ vs. particle momentum.

TABLE III. TPC and TOF selection cuts for K and π tracks.

Variable	$K^{\mp}$	$\pi^{\pm}$
p_T (GeV/c)	> 0.6	0.6
$|\eta|$	< 1.0	1.0
nHitsFit (TPC)	> 20	20
$|n\sigma_X|$	< 2.0	3.0
$|\Delta 1/\beta|$ (if TOF matched)	< 0.03	0.03

ures. 3 and 4 show an example of the particle identification capability from TPC and TOF. Tracks within the kinematic acceptance $p_T > 0.6$ GeV/c and $|\eta| < 1$ are used to combine and make pairs. Table III lists the TPC and TOF selection cuts for daughter kaon and pion tracks used for D^0 reconstruction.

With a pair of two daughter tracks, pion and kaon, the D^0 decay vertex is reconstructed as the middle point on the distance of the closest approach between the two daughter trajectories. The background is mainly due to the random combination of the fake pairs directly from the collision point. With the following topological variables, the background can be greatly reduced.

- Decay Length: the distance between the reconstructed decay vertex and the Primary Vertex (PV, V_z^{TPC}).

- Distance of Closest Approach (DCA) between the 2 daughter tracks (DCA_{12}).

- DCA between the reconstructed D^0 and the PV (DCA_{D^0}).

- DCA between the pion and the PV (DCA_π).

- DCA between the kaon and the PV (DCA_K).

- Angle between D^0 momentum and the line between the reconstructed decay vertex and the PV (θ).

The schematic in Fig. 5 also shows the topological variables used in the analysis, where $\vec{P}$ represent the D^0 momentum. The Decay Length and angle θ follow the formula: $DCA_{D^0} = $ Decay Length $\times \sin(\theta)$. The cuts on the topological variables for this analysis are optimized using a Toolkit for Multivariate Data Analysis (TMVA) package [23], which developed from CERN, in order to have the greatest signal significance. We explored several different discrimination methods in the TMVA package and the Rectangular cut Optimization method is chosen for significance estimation. The optimization is conducted
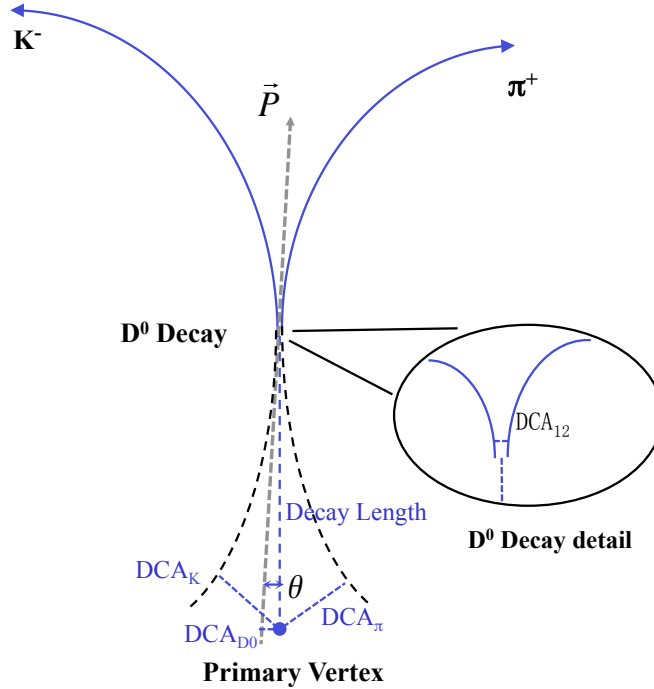
FIG. 5. D^0 topological variables used in the reconstruction.

for different D^0 p_T bins and different centrality bins. Table IV lists a typical set of topological cuts for 0-10% central Au+Au collisions.

Figure 6 shows the invariant mass spectra of $K\pi$ pairs in p_T 0-10 GeV/c and 0-8 GeV/c for three different centralities, 0-80% minimum bias events, 0-10% most central collisions and 60-80% peripheral collisions, respectively. The combinatorial background is estimated with the same event like-sign pairs (grey) and the mixed event unlike-sign (blue) technique in which K and π from different events of similar characteristics (V_Z, centrality, event plane angle) are paired. The mixed event spectra are normalized to the like-sign distributions in the 1.7 to 2.1 GeV/c^2 mass range . After the subtraction of the mixed event combinatorial background from the unlike sign pairs, the rest are shown as red circles in the plot. Compared to the previous D^0 study [12], the D^0 signal significance is largely improved (a factor of ∼15) due to the combinatorial background rejection using the topological cuts enabled by the installation of HFT and optimization with TMVA.

Figures 7 and 8 show the invariant mass spectra at the same centralities as Fig. 6 but for different p_T ranges, Fig. 7 is for the lowest range $0 < p_T < 0.5$ GeV/c and Fig. 8 for the highest range $6 < p_T < 8$ GeV/c.

After the combinatorial background is subtracted, the residual $K\pi$ invariant mass distributions are then fit by a Gaussian plus linear function. The D^0 raw yields are extracted from the fits while the residual background are estimated via the liner function fit.

IV. EFFICIENCIES AND CORRECTIONS

The reconstructed D^0 raw yields are calculated in each centrality, p_T bin, and within the rapidity window $|y| < 1$. The fully corrected D^0 production invariant yields are calculated using the following formula:

$$\frac{d^2N}{2\pi p_T dp_T dy} = \frac{1}{\text{B.R.}} \times \frac{N^{\text{raw}}}{N_{\text{evt}} 2\pi p_T \Delta p_T \Delta y} \times \frac{1}{\varepsilon_{\text{trg}} \times \varepsilon_{\text{TPC}} \times \varepsilon_{\text{HFT}} \times \varepsilon_{\text{PID}} \times \varepsilon_{\text{vtx}}}, \quad (3)$$

where B.R. is the $D^0 \to K^-\pi^+$ decay branching ratio, $(3.89\pm0.04)\%$ [24], N^{raw} is the reconstructed D^0 raw counts, N_{evt} is the total numbers of events used for this analysis, ε_{trg} is the centrality bias correction factor described in Sec. II B. The raw yields need to be corrected for the TPC acceptance and tracking efficiency - ε_{TPC}, the HFT acceptance and tracking plus topological cut efficiency - ε_{HFT}, the particle identification efficiency - ε_{PID}, and the finite vertex resolution correction - ε_{vtx}.

A. TPC Acceptance and Tracking Efficiency - ε_{TPC}

The TPC acceptance and tracking efficiency is obtained using the standard STAR TPC embedding technique, in which a small amount of MC tracks (typically 5% of the total multiplicity of the real event) are processed through the full GEANT simulation [25], then mixed with the raw Data Acquisition (DAQ) data in real

TABLE IV. D^0 topological cuts for the 0-10% most central collisions in separate p_T ranges.

$0 - 10\%$ | p_T (GeV/c)		(0,0.5)	(0.5,1)	(1,2)	(2,3)	(3,5)	(5,8)	(8,10)
Decay Length (μm)	>	100	199	227	232	236	255	255
DCA_{12} (μm)	<	71	64	70	63	82	80	80
DCA_{D^0} (μm)	<	62	55	40	40	40	44	44
DCA_π (μm)	>	133	105	93	97	67	55	55
DCA_K (μm)	>	138	109	82	94	76	54	54
$\cos(\theta)$	>	0.95	0.95	0.95	0.95	0.95	0.95	0.95
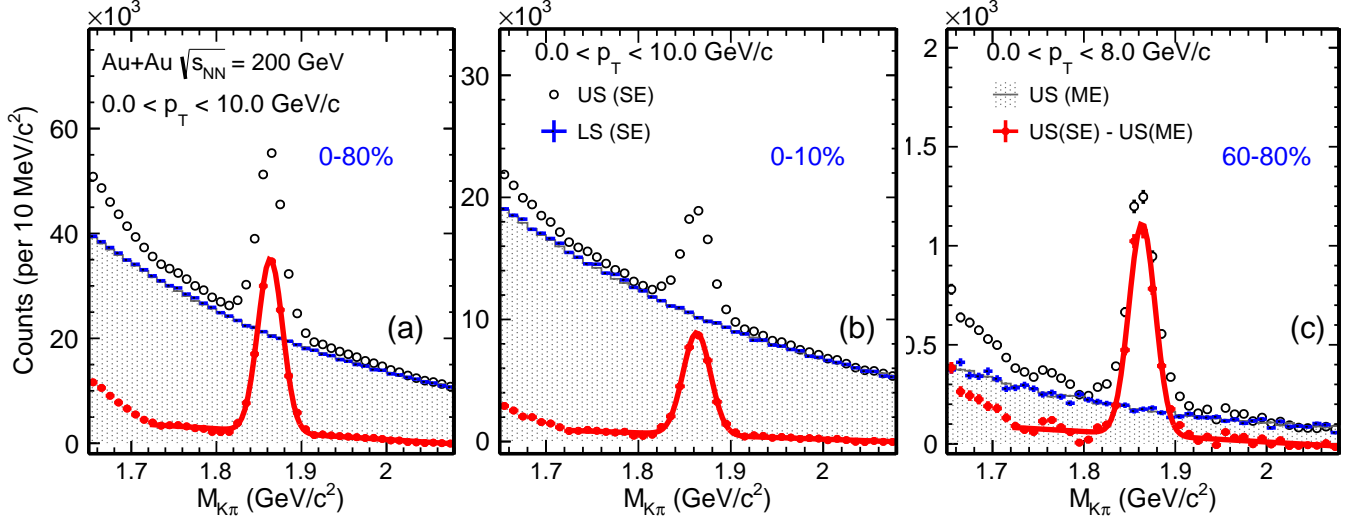
FIG. 6. Invariant mass $M_{K\pi}$ distributions in $0 < p_T < 10$ GeV/c from centrality bins 0–80% (a), 0–10% (b) and $0 < p_T < 8$ GeV/c for 60–80% (c), respectively. The upper limit p_T range for 60–80% stopped at 8 GeV/c since no signal was observed beyond within the current studies. US present unlike-sign pairs while LS represent like-sign pairs. SE present same-event and ME present mixed-event. The hashed region is for ME.

events and reconstructed through the same reconstruction chain as the real data production. The TPC efficiency is then calculated as the ratio of the reconstructed MC tracks with the same offline analysis cuts for geometric acceptance and other TPC requirements to the input MC tracks.

Figure 9 shows the TPC acceptance and tracking efficiency $\varepsilon_{\mathrm{TPC}}$ for D^0 mesons in various centrality classes in this analysis. The efficiencies include the TPC and analysis acceptance cuts $p_T > 0.6 \, \mathrm{GeV}/c$ and $|\eta| < 1$ as well as the TPC tracking efficiency for both pion and kaon daughters. The lower efficiency observed in central collisions is due to the increased multiplicity, and therefore higher occupancy, in these collisions.

B. HFT Acceptance, Tracking and Topological Cut Efficiency - $\varepsilon_{\mathrm{HFT}}$

1. Data-driven Simulation

Since the performance of the HFT changes with time, in order to fully capture the real-time detector performance, the HFT-related efficiency is obtained using a data-driven simulation method in this analysis. The performance of inclusive HFT tracks is characterized by a TPC-to-HFT matching ratio and the DCA distributions. These distributions obtained from real data are fed into a Monte Carlo decay generator for $D^0 \to K^- \pi^+$ and followed by the same reconstruction of D^0 secondary vertex as in real data. The same topological cuts are then applied and the HFT related efficiency for the D^0 reconstruction is calculated.

To best represent the real detector performance, we obtain the following distributions from real data in this Monte Carlo approach.

- Centrality-dependent V_z distributions.

- Ratios of HFT matched tracks to TPC tracks, including the dependence on particle species, centrality, p_T, η, ϕ, and V_z.

- DCA_{XY} - DCA_Z 2-dimensional (2D) distributions including the dependence on particle species, centrality, p_T, η, and V_z.

The DCA_{XY} - DCA_Z 2D distributions are the key to represent not only the right matches, but also the fake matches when connecting the TPC tracks with HFT hits.

FIG. 7. Invariant mass $M_{K\pi}$ distributions in $0 < p_T < 0.5$ GeV/c from centrality bins 0–80% (a), 0–10% (b) and 60–80% (c), respectively. US, LS, SE, ME and the hashed region represent the same meanings as previous plot.

FIG. 8. Invariant mass $M_{K\pi}$ distributions in $6 < p_T < 8$ GeV/c from centrality bins 0–80% (a), 0–10% (b) and 60–80% (c), respectively. US, LS, SE, ME and the hashed region represent the same meaning as previous plot.

The distributions are obtained in 2D to consider the correlation between the two quantities and therefore to reproduce the 3D DCA position distributions. The ϕ dependence of these distributions are integrated over due to computing resource limits, but we have checked the ϕ dependence (by reducing other dependencies for the same reason) and it gives a consistent result compare to the ϕ-integrated one.

In total, there are 11 (ϕ) × 10 (η) × 6 (V_z) × 9 (centrality) × 2 (particles) 1D histograms (36 p_T bins each) used for the HFT match ratio distributions and 5 (η) × 4 (V_z) × 9 (centrality) × 2 (particles) × 19 (p_T) 2D histograms (144 DCA$_{XY}$ × 144 DCA$_Z$ bins) for 2D DCA distributions. The number of bins chosen is optimized to balance the need of computing resources as well as the

stability of the final efficiency. All dimensions have been checked so that further increase in the number of bins (in balance we need to reduce the number of bins in other dimensions) will not change the final obtained efficiency.

The procedure for this data-driven simulation package for efficiency calculation is as follows:

- Sample V_z distribution according to the distribution obtained from the real data.

- Generate D^0 at the event vertex position with desired p_T (Levy shape fitted to D^0 spectra) and rapidity (flat) distributions.

- Propagate D^0 and simulate it's decay to $K^-\pi^+$ daughters following the decay probability.
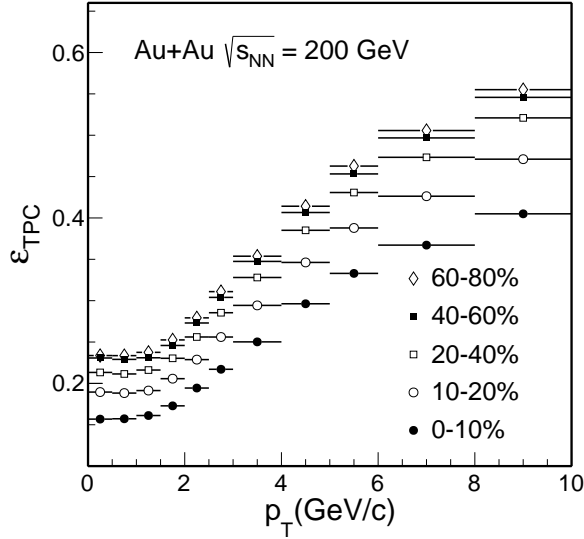
FIG. 9. D^0 TPC acceptance and tracking efficiencies from different centrality classes.

- Smear daughter track momentum according to the values obtained from embedding.

- Smear daughter track starting position according to the DCA_{XY}-DCA_Z 2D distributions from the reconstructed data.

- Apply HFT matching efficiency according to the HFT matching ratio distribution extracted from the reconstructed data.

- Do the topological reconstruction of D^0 decay vertices with the same cuts as applied on data.

The distributions used as input can be obtained from real data or reconstructed data in MC simulation. The latter is used when we validate this approach with the MC GEANT simulation.

This approach assumes these distributions obtained from real data are good representations for tracks produced at or close to the primary vertices. The impact of the secondary particle contribution will be discussed in Sec. IV B 4. The approach also neglects the finite event vertex resolution contribution which will be discussed in Sec. IV C.

Lastly in this MC approach, we also fold in the TPC efficiency obtained from the MC embedding so the following presented efficiency will be the total efficiency of $\varepsilon_{TPC} \times \varepsilon_{HFT}$.

2. Validation with GEANT Simulation

In this subsection, we will demonstrate that the data-driven MC approach has been validated with the GEANT simulation plus the offline tracking reconstruction with realistic HFT detector performance to reproduce the real D^0 reconstruction efficiency.

The GEANT simulation uses the HIJING [26] generator as its input with D^0 particles embedded to enrich the signal statistics. The full HFT detector material including both active and inactive material have been included in the GEANT simulation as well as the offline track reconstruction. The pileup hits in the PXL detector due to finite electronic readout time have been added to realistically represent the HFT match ratio and DCA distributions as shown in Fig. 10.

Figure 10 shows an example of the HFT matching ratio and the 1-D projection of the DCA_{XY} distribution for $1.0 < p_T < 1.2\,\text{GeV}/c$ and 0–10% central collisions. The overall agreements between the GEANT simulation and real data are good. The increase in the HFT matching ratio at low p_T range is due to the increased fake matches (in contrast to truth HFT matches) and the ratio stays flat in the high p_T range. The ratio includes the tracking efficiency when including the HFT hits as well as the HFT geometric acceptance. Therefore the ratio has a strong dependence on the event V_Z and the track η. The DCA distributions used in the package are 2-dimentional distributions, as DCA_{XY} and DCA_Z are strongly correlated.

With the tuned simulation setup (with ideal HFT geometry), we use this sample to validate our data-driven simulation approach for D^0 efficiency calculation. We follow the same procedure as described in Sec. IV B 1 to obtain the HFT match ratio as well as the 2D DCA_{XY}-DCA_Z distributions for primary particles from the reconstructed data. Then the HFT match ratio and 2D DCA distributions are fed into the data-driven simulation to calculate the D^0 reconstruction efficiency. This will be compared to the real D^0 reconstruction efficiency directly obtained from the GEANT simulation sample.

To validate the data-driven simulation tool, Fig. 12 shows an example of the comparisons of several topological variables used in the D^0 reconstruction obtained from the GEANT simulation directly and from the data-driven simulation with the extract distributions from the GEANT simulation as an input in the most central (0–10%) centrality and in $2 < p_T < 3\,\text{GeV}/c$. The topological variables shown here are D^0 decay length, DCA between two D^0 decay daughters, D^0 DCA with respect to the collision vertex, pion DCA and kaon DCA with respect to the collision vertex. As seen in this figure, the data-driven simulation tool reproduces all of these topological distributions quite well. The agreements for the other p_T ranges are also quite good.

Figure 11 shows the D^0 reconstruction efficiency $\varepsilon_{TPC} \times \varepsilon_{HFT}$ calculated with the following two methods in this GEANT simulation. The first method is the standard calculation by applying the tracking and topological cuts for reconstructed D^0 mesons in the simulation sample. In the second method, we employ the data-driven simulation method and take the reconstructed distributions from the simulation sample as an input and then calcu-
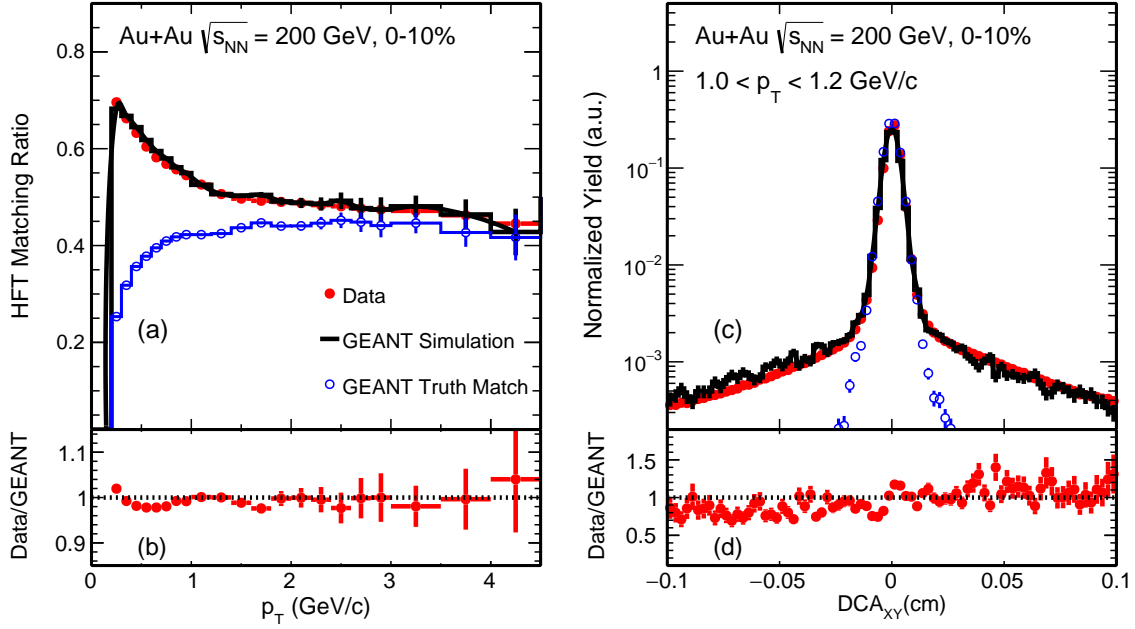
FIG. 10. HFT matching ratio (a) and DCA$_{\text{XY}}$ (c) distributions of inclusive charged pions from real data and MC simulation in 0–10% Au+Au collisions. The ratios between real data and GEANT simulation are shown in the bottom panels and the overall agreements are good. The blue histogram depicts the true matches with HFT hits in the GEANT simulation.
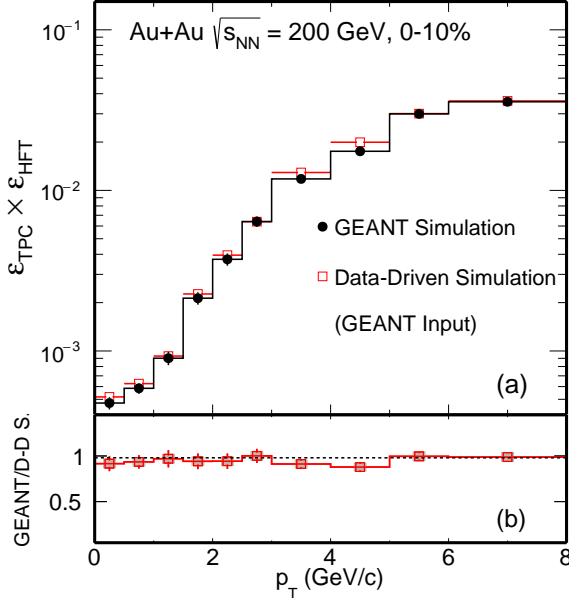

FIG. 11. D^0 reconstruction efficiency comparison between MC simulation (*black*) and data-driven fast simulation with the reconstructed distributions in the simulation sample as an input (*red*) in central 0-10% Au+Au collisions.

late the D^0 reconstruction efficiency in the data-driven simulation framework. In panel (a) of Fig. 11, efficiencies from two calculation methods agree well in the p_T bins in central 0–10% Au+Au collisions, and the ratio between the two is shown in panel (b). This demonstrates that

the data-driven simulation tool can accurately reproduce the real D^0 reconstruction efficiency in central Au+Au collisions.

3. Efficiency for real data

We employ the validated data-driven simulation method for the real data analysis. Figure 13 shows the comparisons of the same five topological variables between D^0 signals in real data and data-driven simulated distributions with real data as an input in central 0–10% collisions for D^0 at $2< p_T <3$ GeV/c. The real data distributions are extracted by reconstructing the D^0 signal with initial cuts (same as the reconstruction cuts in Sec. III, but just remove that particular topological variable as we are going to check) and then statistically subtracting the background distributions using the side-band method. The initial cuts are necessary here to ensure reasonable D^0 signal reconstruction for the extraction of these topological variable distributions, while these pre-cuts effectively reduce the low-end reach for several topological variables, e.g. the D^0 decay length. In the data-driven simulation method, charged pion and kaon HFT matching ratio and 2D DCA distributions are used as an input to calculate these topological variables for D^0 signals. Figure 13 shows that in the selected ranges, the data-driven simulation method reproduces topological variables distributions of D^0 signals, which supports that this method can be reliably used to calculate the topological cut efficiency.
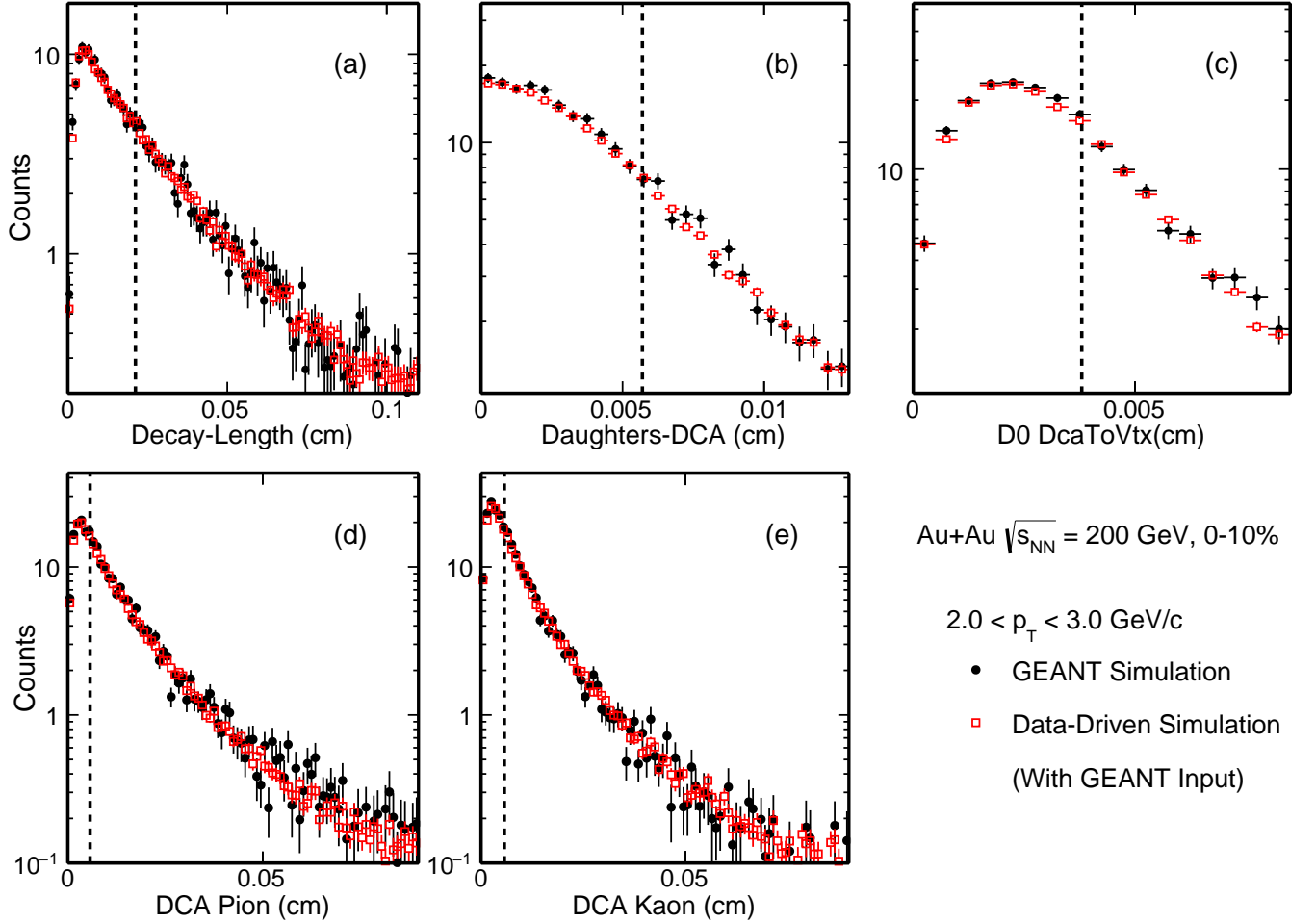
FIG. 12. Topological distributions comparison between MC GEANT simulation (*black*) and data-driven fast simulation with the reconstructed distributions in the simulation sample as an input (*red*) in most central (0–10%) Au+Au collisions.

Figure 14 shows the HFT tracking and topological cut efficiency $\varepsilon_{\mathrm{HFT}}$ as a function of D^0 p_T for different centrality bins obtained using the data-driven simulation method described in this section using the input distributions from the real data. The smaller efficiency seen in central collisions is in part because the HFT tracking efficiency is lower in higher occupancy central collisions, and in addition because we choose tighter topological cuts in central collisions for background suppression.

4. Secondary particle contribution

In the data-driven method for obtaining the efficiency correction, inclusive pion and kaon distributions are taken from real data as an input while the validation with GEANT simulation is perform with primary particles. There is a small amount of secondary contribution (e.g. weak decays from K_S^0 and Λ) to the measured charged pion tracks.

The impact of secondary particle contribution to the charged pions is studied using the HIJING events processed through the GEANT simulation and the same offline reconstruction. The fraction of secondary pions from weak decay of strange hadrons (K_S^0 and Λ) to the total inclusive charged pions within DCA < 1.5 cm cut is estimated to be around 5% at pion $p_T = 0.3\,\mathrm{GeV}/c$ and decrease to be $< 2\%$ above $2\,\mathrm{GeV}/c$. This is consistent with what was observed before in measuring the prompt charged pion spectra [27]. There is another finite contribution of low momentum anti-protons and anti-neutrons annihilated in the detector material and producing secondary pions. The transverse momenta of these pions are mostly around 2–$3\,\mathrm{GeV}/c$ and the fraction of total inclusive pions is $\sim$ 10–12% at p_T = 2-3$\,\mathrm{GeV}/c$ based on this simulation and contribute $\sim$ 5–8% to the HFT matching ratio. This was obtained using the GEANT with GHEISHA hadronic package. With a different hadronic package, FLUKA, the secondary pion fraction in 2–3$\,\mathrm{GeV}/c$ region is significantly reduced and is negligible. The difference between the primary pions and the inclusive pions in the HFT matching ratio has been
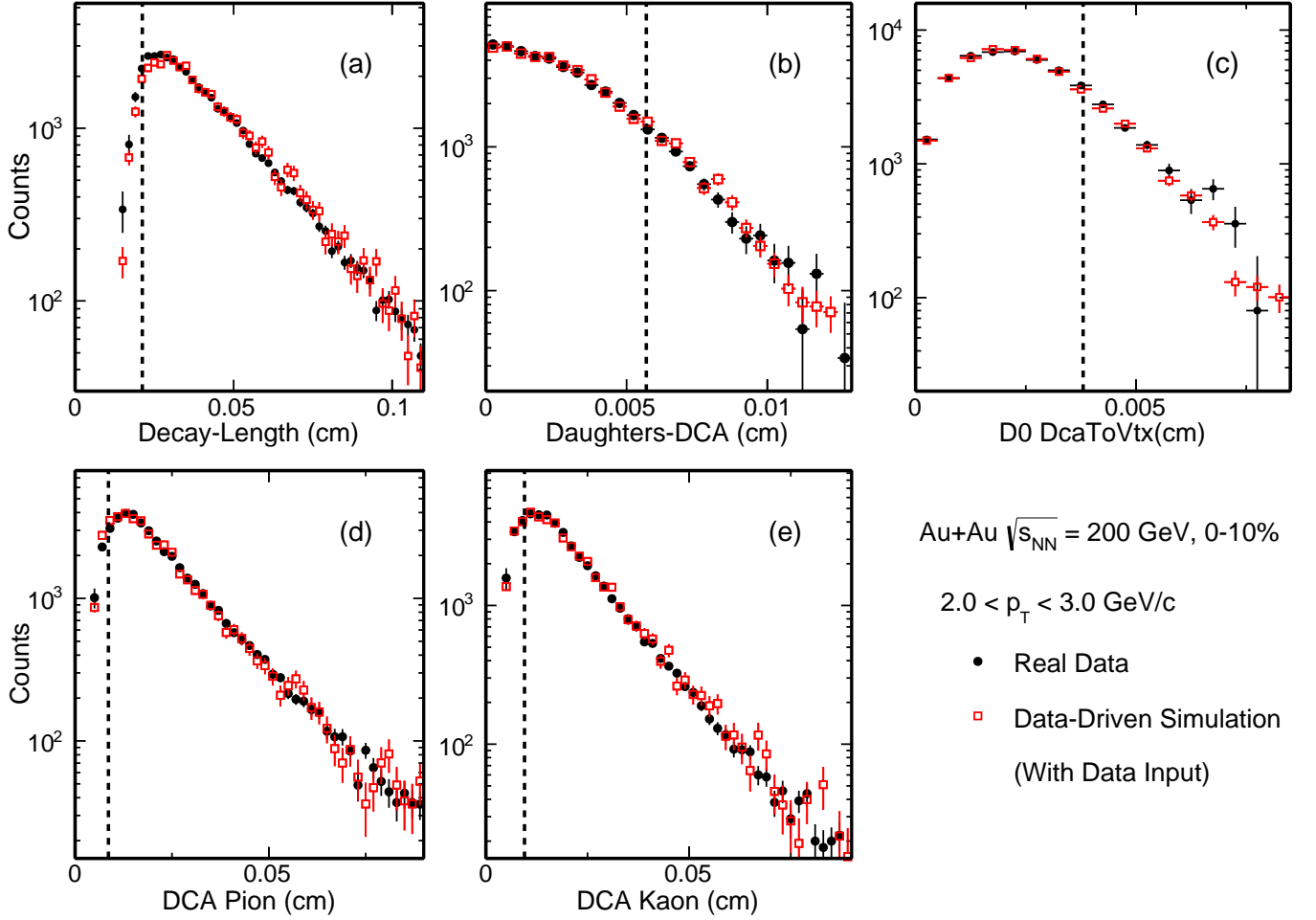
FIG. 13. Comparison of topological variable distributions between D^0 signals in real data (*black*) and in data-driven Simulation with real data distributions as an input (*red*) in most central (0–10%) Au+Au collisions. The dashed lines indicate the final topological cuts chosen for each individual topological variable.

considered as one additional correction factor to take into account these secondary pions in our data-driven simulation method when calculating the efficiency correction, while the maximum difference with respect to the result obtained using the GHEISHA hadronic package is included as the systematic uncertainty for this source. Figure 15 shows the secondary pion contribution in Au+Au collisions. Panel (a) shows the fraction of different sources for secondary tracks including the weak decays, the scatters and the $\bar{p}/\bar{n}$ annihilation. Panel (b) shows the different contributions to the HFT match ratio while panel (c) is the HFT match double ratio which divide the inclusive one to the primary one from panel (b). The effect of such secondary contribution to charged kaons is negligible [27].

C. Vertex Resolution Correction - ε_{vtx}

In the data-driven approach, D^0 mesons are injected at the event vertex. In the real data, the reconstructed vertex has a finite resolution with respect to the real collision vertex. This may have a sizable effect on the reconstructed D^0 signal counts after applying the topological cuts in small multiplicity events where the event vertex resolution decreases. Figure 16 shows the Full-Width-at-Half-Maximum (FWHM) of the difference in the vertex x-position of two randomly-divided sub-events in various centrality bins. We choose the FWHM variable here as the distributions are not particularly Gaussian.

The MC simulation reproduces the vertex difference distributions seen in the real data reasonably well. This gives us confidence in using this MC simulation setup to evaluate the vertex resolution correction ε_{vtx}.

To estimate the vertex resolution effect, we embedded a PYTHIA $c\bar{c}$ event into a HIJING Au+Au event, and ran through the STAR GEANT simulation followed by
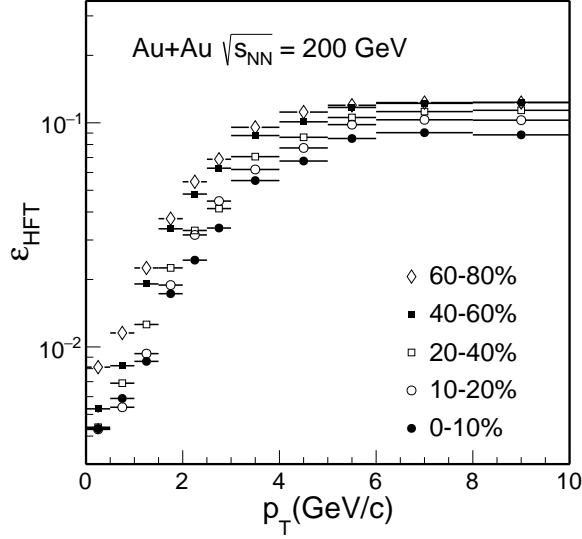
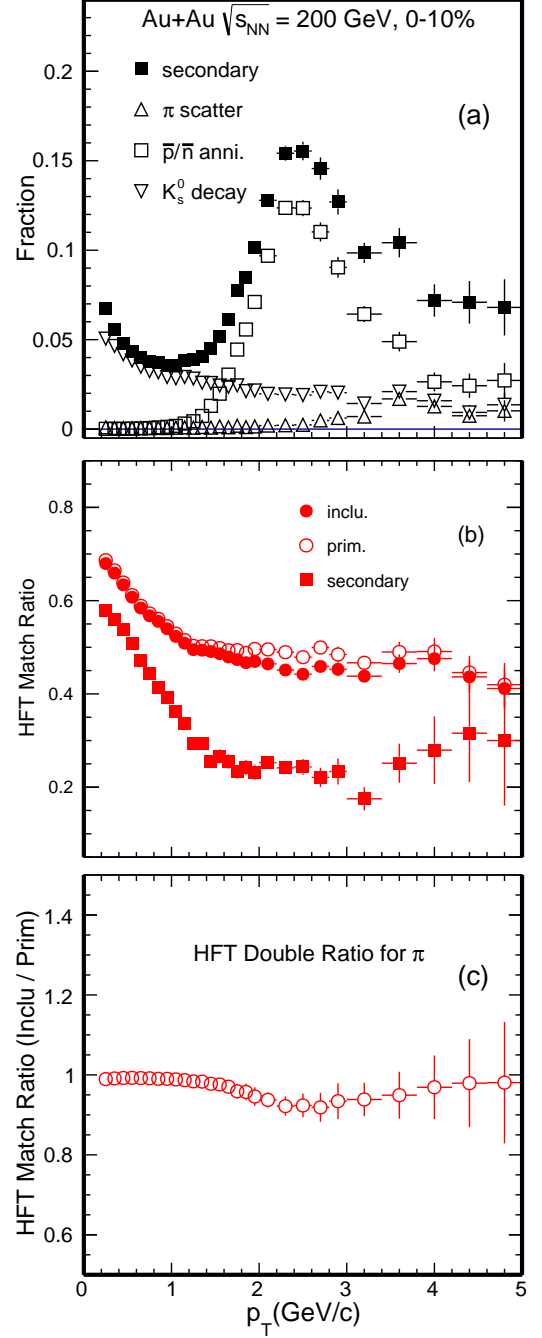FIG. 14. D^0 HFT tracking and topological cut efficiencies from different centrality classes.

FIG. 15. Secondary pion contribution. Panel (a) shows the fraction of different sources for secondary tracks. Panel (b) shows the HFT match ratio while panel (c) shows the HFT match double ratio which divide the inclusive one to the primary one from panel (b).

the same offline reconstruction as in the real data production. The PYTHIA $c\bar{c}$ events are pre-selected to have at least one $D^0 \to K^-\pi^+$ decay or its charge conjugate to enhance the statistics. Figure 17 shows the comparison in the obtained D^0 reconstruction efficiency between MC simulation (*black*) and data-driven simulation using reconstructed distributions in the same MC sample as input (*red*) for 20–30% (left), 50–60% (middle) and 70–80% (right) centrality bins, respectively. The bottom panels show the ratios of the efficiencies obtained from the two calculation methods. In the central and mid-central collisions, the data-driven simulation method can properly reproduce the D^0 real reconstruction efficiency. This is expected since the vertex resolution is small enough so that it has less impact in the obtained efficiency using the data-driven simulation method. However, in more peripheral collisions, the data-driven simulation method overestimates the D^0 reconstruction efficiency as shown in the middle and right panels. The vertex resolution correction factor ε_{vtx}, denotes in Equ. 3, has a mild p_T (2 and 4 GeV/c) dependence but strong centrality dependence in Fig. 18. The brackets denote the systematic uncertainties in the obtained correction factor ε_{vtx}. They are estimated by varying the multiplicity range for the HIJING + GEANT simulation so that the sub-event vertex difference distributions in the real data can be covered by distributions obtained from different simulation samples. The vertex resolution corrections are applied as a function of p_T in each individual centrality class.

D. PID Efficiency - ε_{PID} and Doubly-mis-PID Correction

The D^0 daughter particle identification (PID) cut efficiency includes contributions from the dE/dx selection
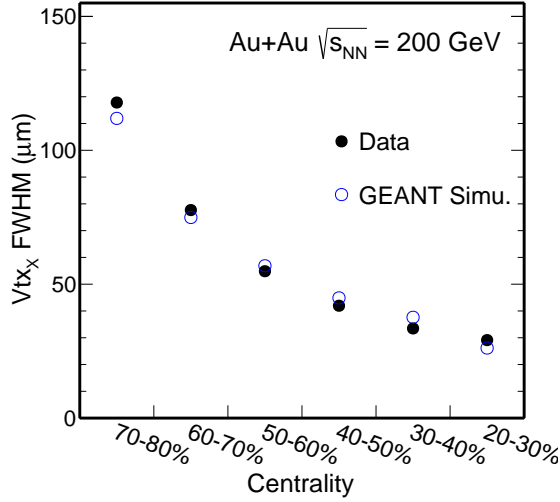
FIG. 16. Full-Width-at-Half-Maximum (FWHM) of vertex position difference in the X dimension between two randomly-divided sub-events in various centrality bins. Black solid circles present the FWHM from real data while the blue empty circles are GEANT simulation.

cut efficiency as well as the TOF matching and $1/\beta$ cut efficiency. To best estimate the selection cut efficiency, we select the pure kaon and pion samples from V0 (ϕ, K_S^0) decay following the same procedure as in [28, 29]. The dE/dx cut efficiencies for pion and kaon daughter tracks are calculated respectively. The TOF $1/\beta$ cut efficiency is determined by studying the $1/\beta$ distributions for kaons and pions in the clean separation region, namely $p_T < 1.5\,\mathrm{GeV}/c$. There is a mild dependence for the offset and width of $\Delta 1/\beta$ distributions vs. particle momentum and our selection cuts are generally wide enough to capture nearly all tracks once they have valid β measurements. The total PID efficiency of D^0 mesons is calculated by folding the individual track TPC and TOF PID efficiencies following the same hybrid PID algorithm as implemented in the data analysis. Figure 19 shows the total PID efficiencies for D^0 reconstruction in various centrality bins. The total PID efficiency is generally high and nearly no centrality or p_T dependence.

When the D^0 daughter kaon track is mis-identified as a pion track and the other daughter pion track is mis-identified as a kaon track, the pair invariant mass distribution will have a bump structure around the real D^0 signal peak, but the distribution is much broader in a wide mass region due to the mis-assigned daughter particle masses. Based on the PID performance study described above, we estimate the single kaon and pion candidate track purities. After folding the realistic particle momentum resolution, we calculate the reconstructed D^0 yield from doubly mis-identified pairs (double counting) underneath the real D^0 signal and the double counting fraction is shown in Fig. 20. The black markers show the fraction by taking all doubly mis-identified pairs in the

D^0 mass window while the blue markers depict it with an additional side-band (SB) subtraction. The latter is used as a correction factor to the central values of reported D^0 yields while the difference between the black and blue symbols is considered the systematic uncertainty in this source. The double counting fraction is below 10% in all p_T bins, and there is little centrality dependence.

Figure 21 shows the total D^0 reconstruction efficiency from different centrality classes in Au+Au collisions including all of the individual components discussed above.

V. SYSTEMATIC UNCERTAINTIES

The systematic uncertainty on the final measured D^0 p_T spectra can be categorized into the uncertainty of the raw D^0 yield extraction and the uncertainty of efficiencies and corrections.

The uncertainty of the raw yield extraction is estimated by a) the difference in the D^0 yield obtained with the fit and bin counting methods, b) varying invariant mass ranges for fit and for side bands and c) varying background estimation from mixed-event and like-sign methods. The maximum difference between these scenarios is then converted to the standard deviation and added to the systematic uncertainties. It is the smallest in the mid-p_T bins due to the best signal significance and grows at both low and high p_T. The double counting contribution in the D^0 raw yield due to mis-PID is included as another contribution to the systematic uncertainty for the D^0 raw yield extraction as described in Sec. IV D.

The uncertainty of the TPC acceptance and efficiency correction $\varepsilon_{\mathrm{TPC}}$ is estimated via the standard procedure in STAR by comparing the TPC track distributions between real data and the embedding data. It is estimated to be $\sim$3–6% for 0-10% collisions and $\sim$3–7% for 60-80% collisions, and is correlated for different centralities and p_T regions.

The uncertainty of the PID efficiency correction is estimated by varying the PID selection cuts and then convolute to the final corrected D^0 yield.

To estimate the uncertainty of the HFT tracking and topological cut efficiency correction $\varepsilon_{\mathrm{HFT}}$, we employ the following procedures: a) We vary the topological variable cuts so the D^0 $\varepsilon_{\mathrm{HFT}}$ is changed to 50% and 150% of the nominal (default) efficiency and compare the efficiency corrected final D^0 yields. The maximum difference between the two scenarios is then added to the systematic uncertainties. b) We also vary the daughter p_T low threshold cut between 0.3 to 0.6 GeV/c and the maximum difference in the final corrected D^0 yield is also included in the systematic uncertainties. c) We add the systematic uncertainty due to limitation of the data-driven simulation approach, $\sim$5%, and the impact of the secondary particles, $\sim$2%, to the total $\varepsilon_{\mathrm{HFT}}$ systematic uncertainty.

With the corrected D^0 transverse momentum spectra, the nuclear modification factor R_{CP} is calculated as the
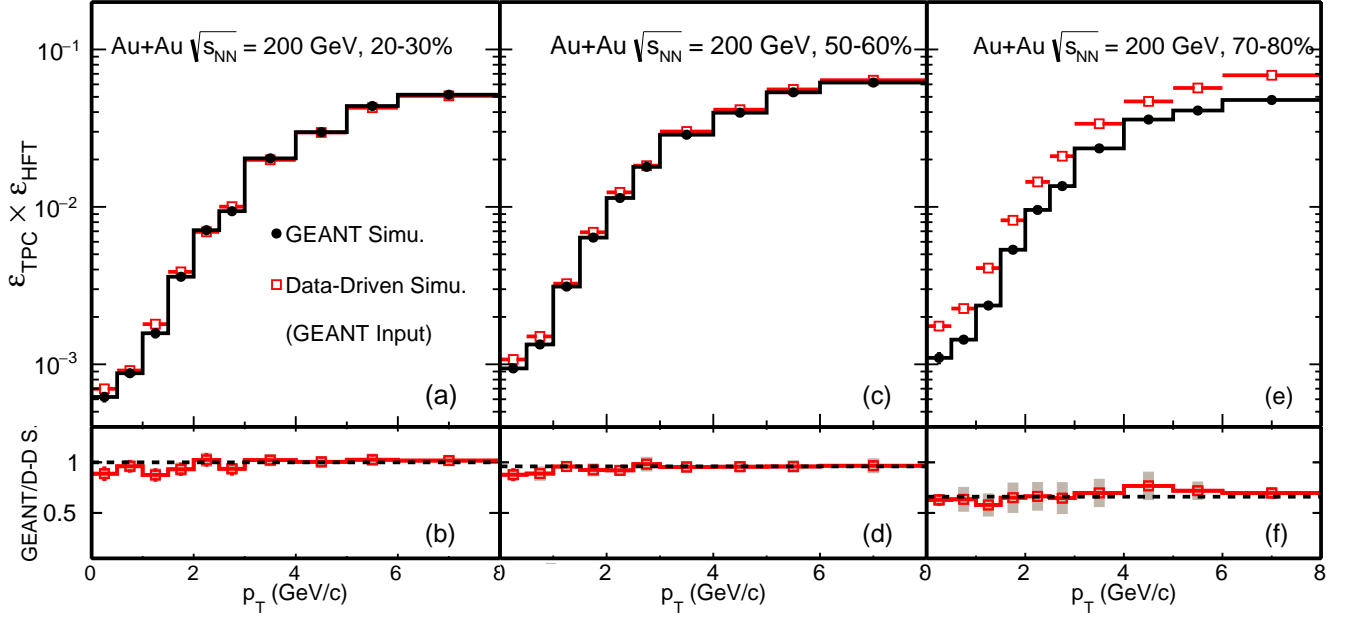
FIG. 17. D^0 reconstruction efficiency comparison between MC GEANT simulation (*black*) and data-driven simulation with the reconstructed distributions in the simulation as an input (*red*) for 20–30% (a,b), 50–60% (c,d) and 70–80% (e,f) Au+Au collisions.
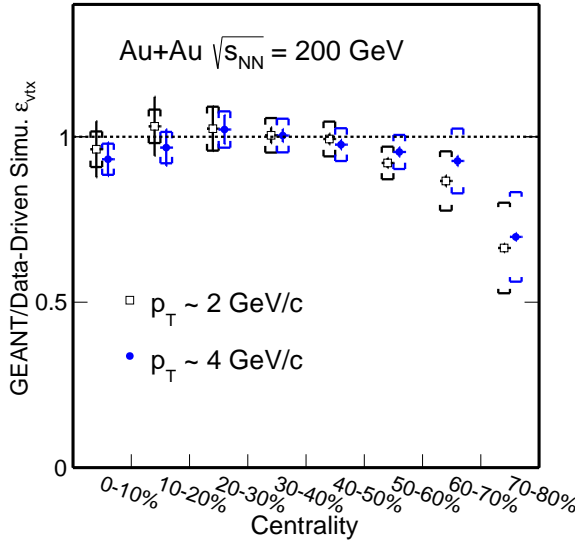

FIG. 18. $\varepsilon_{\rm vtx}$, D^0 reconstruction efficiency ratios between MC GEANT simulation and data-driven simulation with the reconstructed distributions in the simulation as an input versus collision centrality for p_T at 2 and 4 GeV/c. The brackets depict the estimated systematic uncertainties.
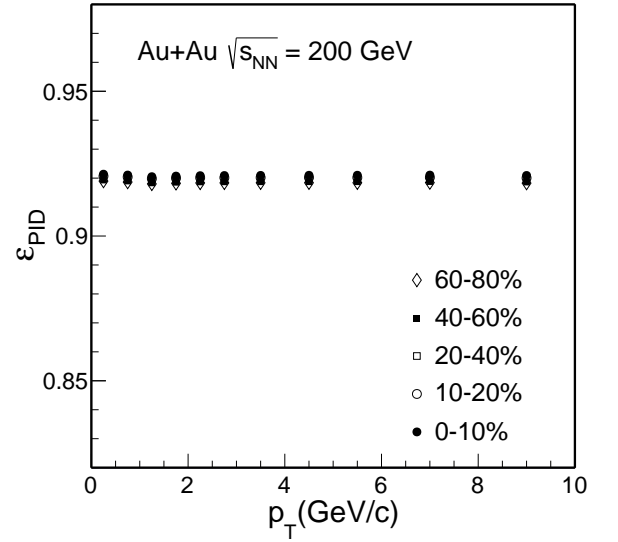
FIG. 19. Particle identification efficiency ($\varepsilon_{\rm PID}$) of D^0 mesons in different centrality classes.

ratio of $N_{\rm bin}$ normalized yields between central and peripheral collisions, as shown in the following formula:

$$R_{\rm CP} = \frac{d^2N/dp_T dy}{N_{\rm bin}}\Big|_{\rm cen} \times \frac{N_{\rm bin}}{d^2N/dp_T dy}\Big|_{\rm peri}. \quad (4)$$

The systematic uncertainties in the raw signal extraction in central and peripheral collisions are propagated as they are uncorrelated, while systematic uncertainties in many other sources are correlated or partially correlated in contributing to the measured D^0 yields. To best consider these correlations, we vary different variables simultaneously in central and peripheral collisions, and the difference in the final extracted $R_{\rm CP}$ value is then directly counted as systematic uncertainties in the measured $R_{\rm CP}$.

FIG. 20. D^0 yield double counting fraction due to doubly mis-PID in different centrality classes. The black markers depict an estimation taking the total double counting yield in the D^0 mass window while the blue markers depict an estimation with an additional side-band (SB) subtraction. No centrality dependence observed.
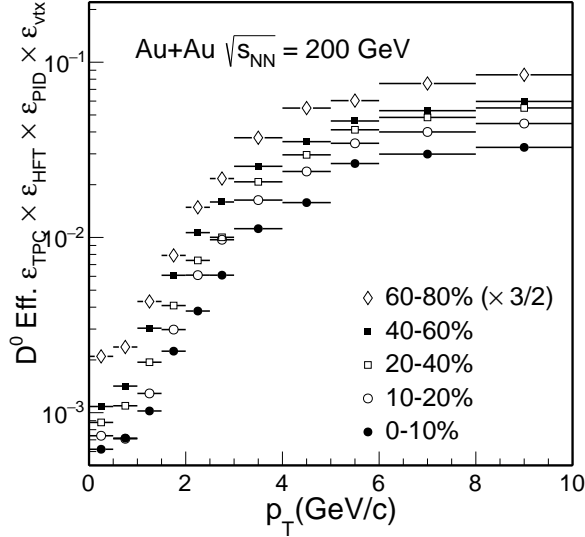

FIG. 21. The total D^0 reconstruction efficiency from different centrality classes.

The nuclear modification factor R_{AA} is calculated as the ratio of N_{bin} normalized yields between Au+Au and $p+p$ collisions. The baseline chosen and uncertainty sources for $p+p$ collisions are the same as the publication [12]. The uncertainties from the $p+p$ reference dominates this systematic uncertainty, which include the 1σ uncertainty from the Levy fit and the difference between Levy and power-law function fits for extrapolation to low and high p_T, expressed as 1 standard deviation.

With the corrected D^0 and $\overline{D}^0$ transverse momentum spectra, the $\overline{D}^0/D^0$ ratio is calculated as a function of the transverse momentum. The systematic uncertainties in the raw signal extraction for $\overline{D}^0$ and D^0 are propagated as they are uncorrelated, while systematic uncertainties in many other sources are correlated or partially correlated in contributing to the measured $\overline{D}^0/D^0$ ratio. As in the R_{CP} systematic uncertainty estimation, we vary different variables simultaneously for D^0 and $\overline{D}^0$, and the difference in the final extracted $\overline{D}^0/D^0$ value is then directly counted as systematic uncertainties in the measured $\overline{D}^0/D^0$.

Table V summarizes the systematic uncertainties and their contributions, in percentage, on the D^0 invariant yield in 0-10% and 60-80% collisions and R_{CP}(0-10%/60-80%). In the last column we also comment on the correlation in p_T for each individual source. Later when reporting p_T integrated yields or R_{CP}, systematic uncertainties are calculated under the following considerations: a) for p_T uncorrelated sources, we take the quadratic sum of various p_T bins; b) for sources that are largely correlated in p_T, we take the arithmetic sum as a conservative estimate.

VI. RESULTS AND DISCUSSION

A. p_T Spectra and Integrated Yields

Figure 22 shows the efficiency-corrected D^0 invariant yield at mid-rapidity ($|y| < 1$) vs. p_T in 0–10%, 10–20%, 20–40%, 40–60% and 60–80% Au+Au collisions. D^0 spectra in some centrality bins are arbitrarily scaled with factors indicated on the plot for clarity. Dashed and solid lines depict fits to the spectra with the Levy function:

$$\frac{d^2N}{2\pi p_T dp_T dy} = \frac{1}{2\pi}\frac{dN}{dy}\frac{(n-1)(n-2)}{nT(nT+m_0(n-2))} \times \left(1+\frac{\sqrt{p_T^2+m_0^2}-m_0}{nT}\right)^{-n}, \quad (5)$$

where m_0 is the D^0 mass (1.864 GeV/c^2) and $\frac{dN}{dy}$, T and n are free parameters. The Levy function fit describes the D^0 spectra nicely in all centrality bins up to 8 GeV/c.

We compare our new measurements with previous measurements using the STAR TPC only. The previous measurements are recently corrected after fixing errors in the TOF PID efficiency calculation [12]. Figure 23 shows the p_T spectra comparison in 0–10%, 10-40% and 40–80% centrality bins in panel (a) and the ratios to the Levy fit functions in panels (b), (c), and (d). The new measurement with the HFT detector shows a nice agreement with the measurement without the HFT, but with significantly improved precision.

TABLE V. Summary of systematic uncertainties, in percentage, on the D^0 invariant yield in 0-10% and 60-80% collisions and $R_{\rm CP}(0\text{-}10\%/60\text{-}80\%)$.

Source	Systematic uncertainty [%]			Correlation in p_T
	0–10%	60–80%	$R_{\rm CP}(0\text{-}10\%/60\text{-}80\%)$	
Signal extra.	1-6	1-12	2-13	uncorr.
Double mis-PID	1-7	1-7	negligible	uncorr.
$\varepsilon_{\rm TPC}$	5-7	5-8	3-7	largely corr.
$\varepsilon_{\rm HFT}$	3-15	3-20	3-20	largely corr.
$\varepsilon_{\rm PID}$	3	3	negligible	largely corr.
$\varepsilon_{\rm vtx}$	5	9-18	10-18	largely corr.
BR.	0.5		0	global
$N_{\rm bin}$	2.8	42	42	global
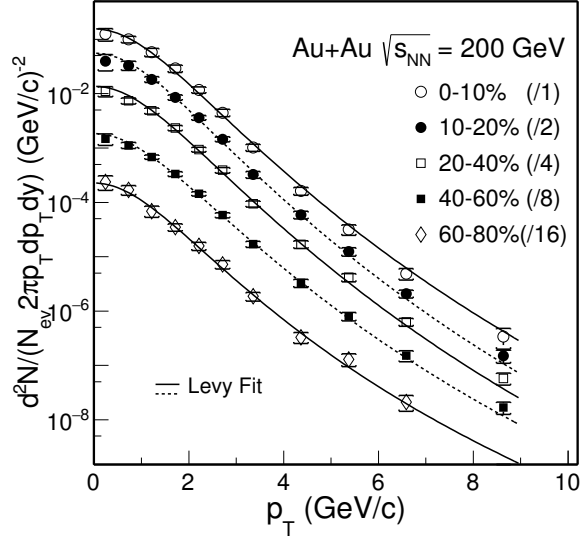
FIG. 22. D^0 invariant yield at mid-rapidity ($|y| < 1$) vs. transverse momentum for different centrality classes. Error bars (not visible for many data points) indicate statistical uncertainties and brackets depict systematic uncertainties. Global systematic uncertainties in $B.R.$ are not plotted. Solid and dashed lines depict Levy function fits.

The measured D^0 spectra cover a wide p_T region which allows us to extract the p_T integrated total D^0 yield at mid-rapidity with good precision. Figure 24 shows the p_T integrated cross section $d\sigma^{NN}/dy|_{y=0}$ for D^0 production per nucleon-nucleon collision from different centrality bins for the full p_T range shown in the top panel and for $p_T > 4\,{\rm GeV}/c$ shown in the bottom panel. The result from a previous $p+p$ measurement is also shown in the top panel.

The total D^0 cross section per nucleon-nucleon collision at mid-rapidity $d\sigma^{NN}/dy|_{y=0}$ shows approximately a flat distribution as a function of $N_{\rm part}$, even though the systematic uncertainty in the 60–80% centrality bin is a bit large. The values in mid-central to central Au+Au collisions are smaller than that in $p+p$ collisions with $\sim 1.5\sigma$ effect considering the large uncertainties from

FIG. 23. (a) Measured D^0 spectra from this analysis compared with the previous 2010/11 measurements for different centrality classes. Dashed lines depict Levy function fits to 2014 data. (b) - (d), Ratio of measured spectra to the fitted Levy function.

the $p+p$ measurements. The total charm quark yield in heavy-ion collisions is expected to follow the number-of-binary-collision scaling since charm quarks are believed to be predominantly created at the initial hard scattering before the formation of the QGP at RHIC energies. However, the cold nuclear matter (CNM) effect including shadowing could also play an important role. In ad-
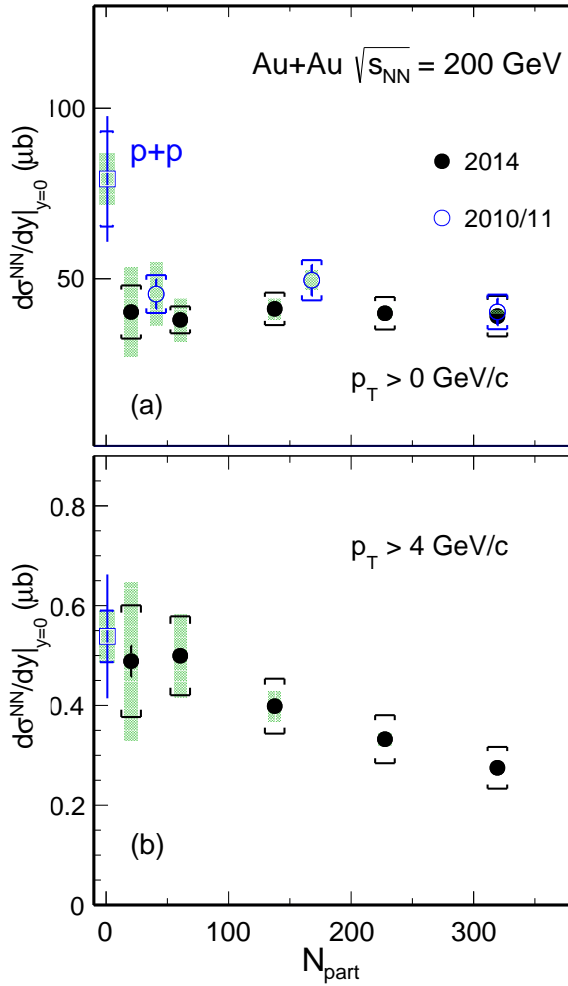
FIG. 24. Integrated D^0 cross section at mid-rapidity per nucleon-nucleon collision at mid-rapidity for $p_T > 0$ (a) and $p_T > 4\,\mathrm{GeV}/c$ (b) as a function of centrality N_{part}. The statistical and systematic uncertainties are shown as error bars and brackets on the data points. The green boxes on the data points depict the overall normalization uncertainties in $p+p$ and Au+Au data respectively.
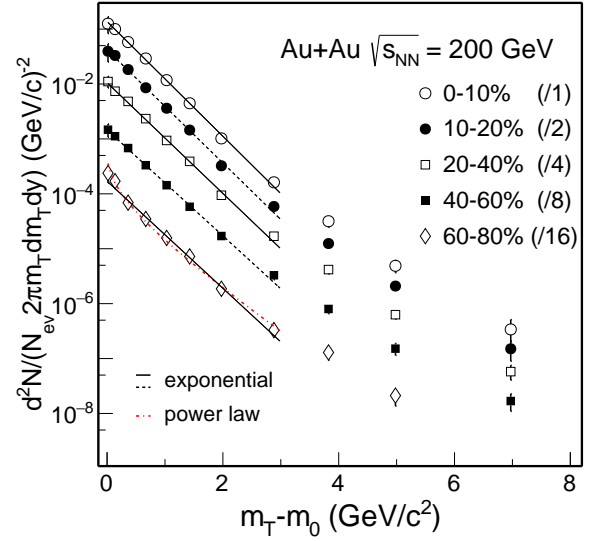

FIG. 25. D^0 invariant yield at mid-rapidity ($|y| < 1$) vs. transverse kinetic energy (m_T - m_0) for different centrality classes. Error bars (not visible for many data points) indicate statistical uncertainties and brackets depict systematic uncertainties. Global systematic uncertainties in $B.R.$ are not plotted. Solid and dashed black lines depict exponential function fits and the dot-dashed line depict a power-law function fit to the spectrum in 60–80% centrality bin.

B. Collectivity

1. m_T Spectra

Transverse mass spectra can be used to study the collectivity of produced hadrons in heavy-ion collisions. Figure 25 shows the D^0 invariant yield at mid-rapidity ($|y| < 1$) vs. transverse kinetic energy (m_T - m_0) for different centrality classes, where $m_T = \sqrt{p_T^2 + m_0^2}$ and m_0 is the D^0 meson mass. Solid and dashed black lines depict thermal model inspired exponential function fits to data in various centrality bins up to $m_T - m_0 < 3\,\mathrm{GeV}/c^2$ using the fit function shown below:

$$\frac{d^2 N}{2\pi m_T dm_T dy} = \frac{dN/dy}{2\pi T_{\mathrm{eff}}(m_0 + T_{\mathrm{eff}})} e^{-(m_T - m_0)/T_{\mathrm{eff}}}. \quad (6)$$

Such a method has been often used to analyze the particle spectra and to understand kinetic freezeout properties for the data in heavy–ion collisions [1, 33].

A power-law function (shown below) is also used to fit the spectrum in the 60–80% centrality bin:

$$\frac{d^2 N}{2\pi p_T dp_T dy} = \frac{dN}{dy} \frac{4(n-1)(n-2)}{2\pi(n-3)^2 \langle p_T \rangle^2} \left(1 + \frac{2p_T}{\langle p_T \rangle(n-3)}\right)^{-n}, \quad (7)$$

where dN/dy, $\langle p_T \rangle$, and n are three free parameters.

The power-law function fit shows a good description of the 60–80% centrality data indicating that the D^0 meson production in this peripheral bin is close to the expected

dition, hadronization through coalescence has been suggested to potentially modify the charm quark distribution in various charm hadron states which may lead to the reduction in the observed D^0 yields in Au+Au collisions [30] (as seen in Fig. 24). For instance, hadronization through coalescence can lead to an enhancement of the charmed baryon Λ_c^+ yield relative to D^0 yield [31], and together with the strangeness enhancement in the hot QCD medium, can also lead to an enhancement in the charmed strange meson D_s^+ yield relative to D^0 [32]. Therefore, determination of the total charm quark yield in heavy-ion collisions will require measurements of other charm hadron states over a broad momentum range.

feature of perturbative QCD. The D^0 meson spectra in more central collisions can be well described by the exponential function fit at m_T - $m_0 < 3\,\mathrm{GeV}/c^2$ suggesting the D^0 mesons have gained collective motion in the medium evolution in these collisions.

The obtained slope parameter T_{eff} for D^0 mesons is compared to other light and strange hadrons measured at RHIC. Figure 26 summarizes the slope parameter T_{eff} for various identified hadrons ($\pi^\pm$, $K^\pm$, $p/\bar{p}$, ϕ, Λ, Ξ^-, Ω, D^0 and J/ψ) in central Au+Au collisions at $\sqrt{s_{\mathrm{NN}}} = 200\,\mathrm{GeV}$. Point-by-point statistical and systematic uncertainties are added as a quadratic sum when performing these fits. All fits are performed up to $m_T - m_0 < 1\,\mathrm{GeV/c^2}$ (π, K, p), $< 2\,\mathrm{GeV}/c^2$ (ϕ, Λ, Ξ), $< 3\,\mathrm{GeV}/c^2$(Ω, D^0, J/ψ) for each particle, respectively.

The slope parameter T_{eff} in a thermalized medium can be characterized by the random (generally interpreted as a kinetic freezeout temperature T_{fo}) and collective (radial flow velocity $\langle\beta_T\rangle$) components with a simple relation [1, 34, 35]:

$$T_{\mathrm{eff}} = T_{\mathrm{fo}} + m_0\langle\beta_T\rangle^2, \tag{8}$$

therefore, T_{eff} will show a linear dependence as a function of particle mass m_0 with a slope that can be used to characterize the radial flow collective velocity.

The data points clearly show two different systematic trends. π, K, p data points follow one linear dependence while ϕ, Λ, Ξ^-, Ω^-, D^0 data points follow another linear dependence, as represented by the dashed lines shown in Fig. 26. Particles, such as, π, K, p gain radial collectivity through the whole system evolution, therefore the linear dependence exhibits a larger slope. On the other hand the linear dependence of ϕ, Λ, Ξ^-, Ω^-, D^0 data points shows a smaller slope indicating these particles may freeze out from the system earlier, and therefore receive less radial collectivity.

2. Blast-wave fit

The Blast-Wave (BW) model is extensively used to study the particle kinetic freeze-out properties. Assuming a hard-sphere uniform particle source with a kinetic freeze-out temperature T_{kin} and a transverse radial flow velocity β, the particle transverse momentum spectral shape is given by [36]:

$$\frac{dN}{p_T dp_T} = \frac{dN}{m_T dm_T} \propto$$
$$\int_0^R r\,dr\,m_T I_0\left(\frac{p_T \sinh\rho}{T_{\mathrm{kin}}}\right) K_1\left(\frac{m_T \cosh\rho}{T_{\mathrm{kin}}}\right), \tag{9}$$

where $\rho = \tanh^{-1}\beta$, and I_0 and K_1 are the modified Bessel functions. The flow velocity profile is taken as:

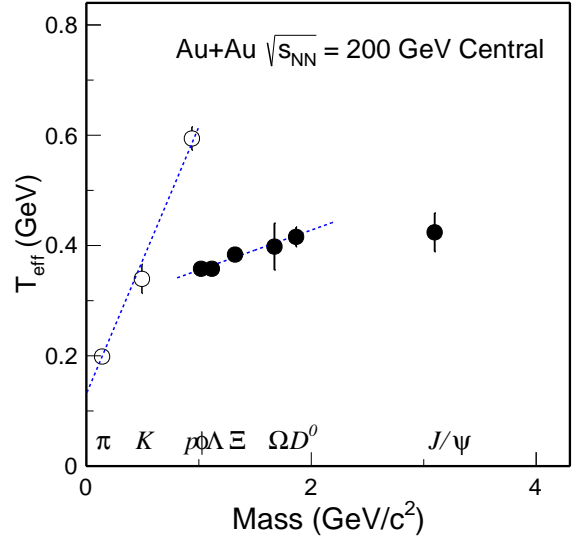$$\beta = \beta_S \left(\frac{r}{R}\right)^n, \tag{10}$$

FIG. 26. Slope parameter T_{eff} for different particles in central Au+Au collisions. The dashed lines depict linear function fits to π, K, p and $\phi, \Lambda, \Xi^-, \Omega^-, D^0$ respectively.
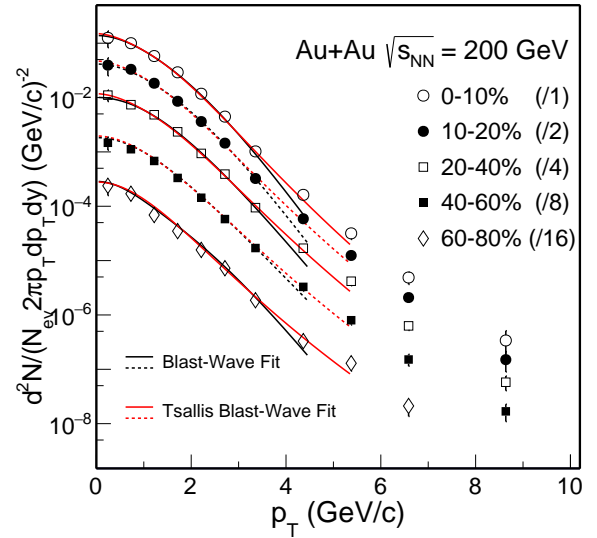

FIG. 27. D^0 invariant yield at mid-rapidity ($|y| < 1$) vs. transverse momentum for different centrality classes. Black lines depict Blast-Wave function and red lines are Tsallis Blast-Wave (TBW) fits.

where β_S is the maximum velocity at the surface and r/R is the relative radial position in the thermal source. The choice of R only affects the overall spectrum magnitude while the spectrum shape constrains the three free parameters T_{kin}, $\langle\beta\rangle = 2/(2+n)\beta_S$, and n.

Figure 27 shows the Blast-Wave and Tsallis Blast-Wave (TBW) fits to the data in different centrality bins. The n parameter in these fits are fixed to be 1 due to the limited number of data points and is inspired by the fit result for light-flavor hadrons (π, K, p) [37]. The p_T
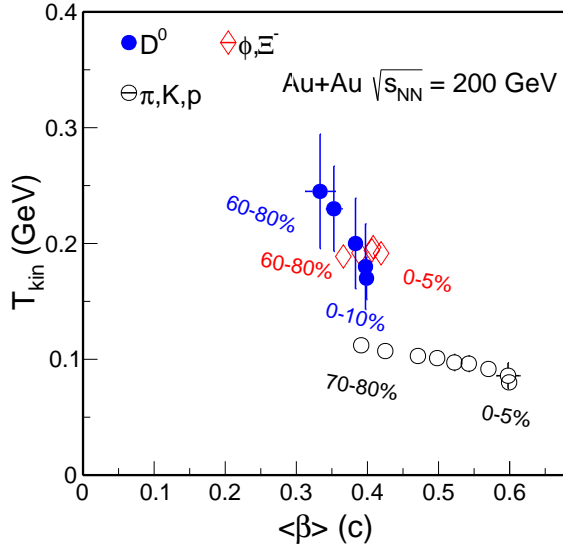
FIG. 28. Results of T_{kin} vs. $\langle\beta\rangle$ from the Blast-Wave model fits to different groups of particles. The data points for each group of particles present the results from different centrality bins with the most central data point at the largest $\langle\beta\rangle$.

range in the BW fits is restricted to be less than $3m_0$ where m_0 is the rest mass of D^0 mesons.

Figure 28 summarizes the fit parameters T_{kin} vs. $\langle\beta\rangle$ from the Blast-Wave model fits to different groups of par- ticles: black markers for the simultaneous fit to π, K, p; red markers for the simultaneous fit to ϕ, Ξ^- and blue markers for the fit to D^0. The data points for each group of particles represent the fit results from differ- ent centrality bins with the most central data point at the largest $\langle\beta\rangle$ value. Similar as in the fit to the m_{T} spectra, point-by-point statistical and systematic uncer- tainties are added in quadrature when performing the fit. The fit results for π, K, p are consistent with pre- viously published results [37]. The fit results for multi- strangeness particles ϕ, Ξ^- and D^0 show much smaller mean transverse velocity $\langle\beta\rangle$ and larger kinetic freeze-out temperature. Which is consistent with particle freeze out earlier from the system and gain less radial collec- tivity. The resulting T_{kin} parameters for ϕ, Ξ^- and for D^0 are close to the critical temperature T_{C} (likely, of about 160 MeV) indicating negligible contribution from the hadronic stage to the observed radial flow of these particles. The collectivity they obtain is mostly through the partonic stage re-scatterings in the QGP phase.

The TBW fit accounts for non-equilibrium features in a system with an additional parameter q [37]. Table VI lists the fitting parameters, $\langle\beta\rangle$ and $(q-1)$ for the D^0 data in different centralities. Results show a similar trend as the regular BW fit, i.e. the most central data point is located at the largest $\langle\beta\rangle$ value. The $(q-1)$ parameter in TBW, which characterizes the degree of non-equilibrium in a system, indicates a decreasing trend from periph- eral to central collisions, indicating that the system is

TABLE VI. $\langle\beta\rangle$ and $(q-1)$ from the Tsallis Blast-Wave fits to the D^0 data in different centralities .

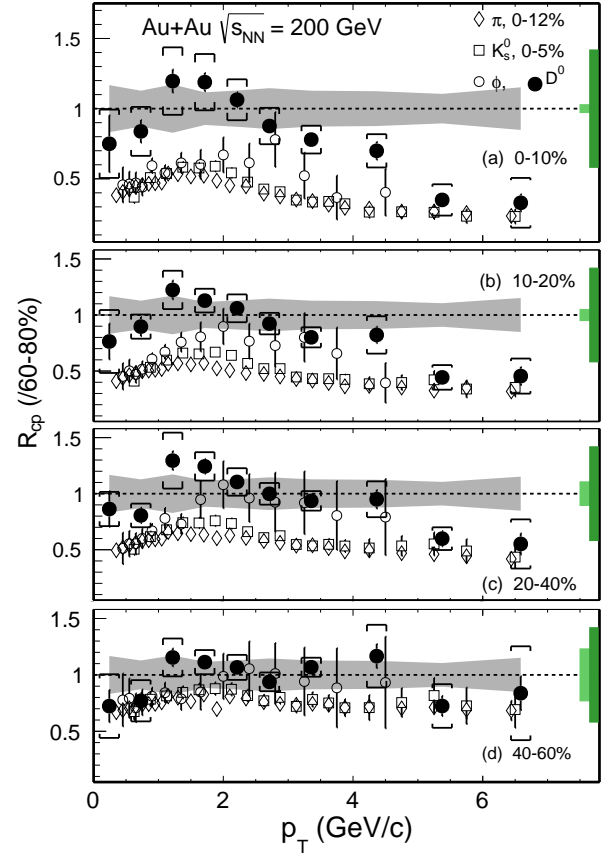| Centrality	$\langle\beta\rangle(c)$	$q-1$
0–10 %	0.263 ± 0.018	0.066 ± 0.008
10–20 %	0.255 ± 0.022	0.068 ± 0.010
20–40 %	0.264 ± 0.015	0.070 ± 0.007
40–60 %	0.251 ± 0.023	0.074 ± 0.011
60–80 %	0.217 ± 0.037	0.075 ± 0.010

FIG. 29. D^0 R_{CP} with the 60–80% spectrum as the reference for different centrality classes in Au+Au collisions compared to that of other light and strange mesons ($\pi^{\pm}$, K_S^0 and ϕ) [38– 40]. The statistical and systematic uncertainties are shown as error bars and brackets on the data points. The grey bands around unity depict the systematic uncertainty due to vertex resolution correction, mostly from the 60–80% reference spec- trum. The light and dark green boxes on the right depict the normalization uncertainty in determining the N_{bin}.

approaching thermalization in more central collisions.

C. Nuclear Modification Factor - R_{CP} and R_{AA}

Figure 29 shows the calculated R_{CP} with the 60–80% peripheral bin as the reference for different centrality bins 0–10%, 10–20%, 20–40% and 40–60% and is compared to

other light and strange flavor mesons. The grey bands around unity depict the vertex resolution correction uncertainty on the measured D^0 data points, mostly originating from the 60–80% reference spectrum. The dark and light green boxes around unity on the right side indicate the global $N_{\rm bin}$ systematic uncertainties for the 60–80% centrality bin and for the corresponding centrality bin in each panel. The global $N_{\rm bin}$ systematic uncertainties should be applied to the data points of all particles in each panel.

The measured D^0 $R_{\rm CP}$ in central 0–10% collisions shows a significant suppression at $p_T > 5\,{\rm GeV}/c$. The suppression level is similar to that of light and strange flavor mesons and the $R_{\rm CP}$ suppression gradually decreases when moving towards from central collisions to mid-central and peripheral collisions. The D^0 $R_{\rm CP}$ for $p_T < 4\,{\rm GeV}/c$ is consistent with no suppression, in contrast to light-flavor hadrons. This structure is consistent with the expectation from model predictions that charm quarks gain sizable collective motion during the medium evolution. Comparisons to dynamic model calculations for the D^0 $R_{\rm CP}$ will be discussed in the next Sec. VI E.

The precision of the 60–80% centrality spectrum is limited due to the large systematic uncertainty in determining the $N_{\rm bin}$ based on the MC Glauber model. Figure 30 shows the D^0 $R_{\rm CP}$ for different centralities as a function of p_T with the 40–60% centrality spectrum as the reference. The grey band around unity in the top panel is the vertex contribution for the systematic uncertainties from the 40–60% centrality. The green boxes around unity depict the global $N_{\rm bin}$ systematic uncertainties for the 40–60% centrality bin and for each corresponding centrality bin. As a comparison, $R_{\rm CP}$ of charged pions, K_s^0 and ϕ in the corresponding centralities are also plotted in each panel. With much smaller systematic uncertainties, the observations seen before using the 60–80% centrality spectrum as the reference still hold.

Figure 31 shows the calculated $R_{\rm AA}$ with the $p+p$ measurement [20] as the reference for different centrality bins 0–10% (a), 10–40% (b) and 40–80% (c) and compared with the previous Au+Au measurements using the STAR TPC after the recent correction [12]. The $p+p$ D^0 reference spectrum is updated using the latest global analysis of charm fragmentation ratios from [44] and also by taking into account the p_T dependence of the fragmentation ratio between D^0 and $D^{*\pm}$ from PYTHIA. The new measurement with the HFT detector shows a nice agreement with the measurement without the HFT, but with much improved precision. The grey bands around each data point depict the $p+p$ systematic uncertainty on the measured D^0 data points. The first two and last two data points are empty circles indicating those are calculated with an extrapolated $p+p$ reference. The dark and light green boxes around unity on the right side indicate the global $N_{\rm bin}$ systematic uncertainties for the corresponding centrality bin in each panel and the global cross sectional uncertainties from $p+p$.

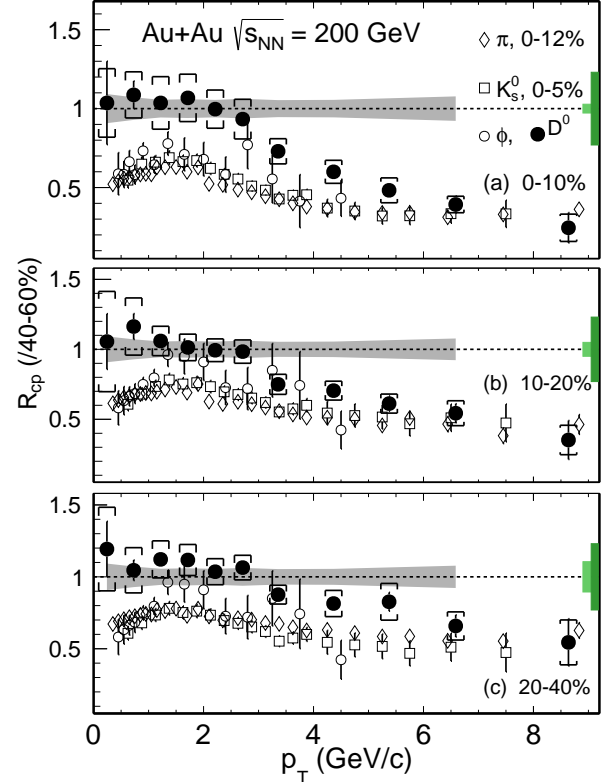The measured D^0 $R_{\rm AA}$ in central (0-10%) and mid-

FIG. 30. D^0 $R_{\rm CP}$ with the 40–60% spectrum as the reference for different centrality classes in Au+Au collisions compared to that of other light and strange mesons ($\pi^{\pm}$, K_S^0 and ϕ) [38–40]. The statistical and systematic uncertainties are shown as error bars and brackets on the data points. The grey bands around unity depict the systematic uncertainty due to vertex resolution correction, mostly from the 40–60% reference spectrum. The light and dark green boxes on the right depict the normalization uncertainty in determining the $N_{\rm bin}$.

central (10-40%) collisions show a significant suppression at the high p_T range which reaffirms the strong interactions between charm quarks and the medium, while the new Au+Au data points from this analysis contain much improved precision. Figure 32 shows the D^0 $R_{\rm AA}$ in the 0-10% most central collisions compared to that of (a) average D meson from ALICE and (b) charged hadron from ALICE and $\pi^{\pm}$ from STAR [10, 45, 46]. The comparison of D^0 suppression between STAR and ALICE shows reasonable agreement within the uncertainties despite the large energy difference from $200\,{\rm GeV}$ to $2.76\,{\rm TeV}$. The comparison to that of light hadrons shows similar suppression at the high p_T, while in the intermediate range, D^0 mesons are less suppressed.
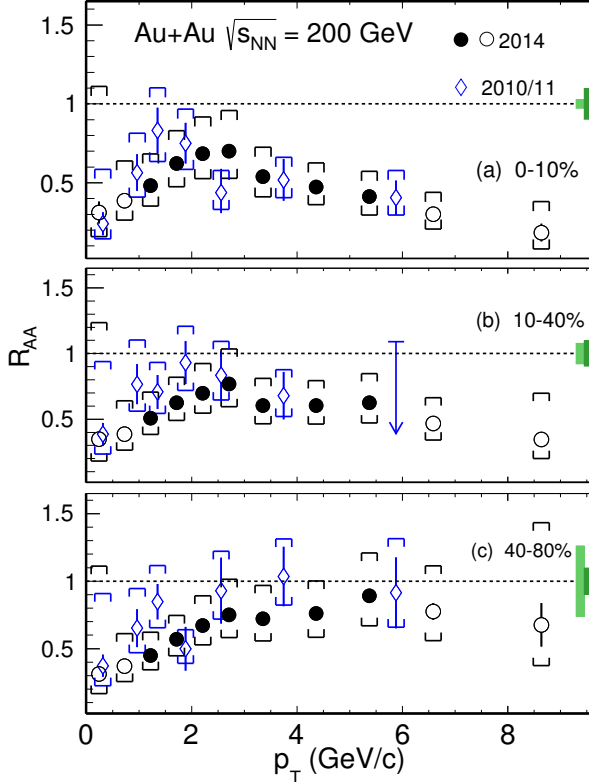
FIG. 31. D^0 R_{AA} with the $p+p$ spectrum as the reference for different centrality classes. The first two and last two data points are presented as empty circles, indicating that the $p+p$ reference is extrapolated into these p_T ranges. The statistical and systematic uncertainties are shown as error bars and brackets on the data points. The light and dark green boxes on the right depict the normalization uncertainty in determining the N_{bin} and cross sectional from $p+p$.

D. $\overline{D}^0$ and D^0 spectra and double ratio

Figure 33 shows the p_T spectra comparison between $\overline{D}^0$ and D^0 in 0–10%, 10–20%, 20–40%, 40–60% and 60–80% centrality bins. Figure 34 shows the $\overline{D}^0/D^0$ ratio in the corresponding centrality bins. With the current data, the $\overline{D}^0$ yield is significantly larger than the D^0 in the most central and mid-central collisions. With the consideration of the statistical and systematic uncertainties, a constant fit is performed to quantify the deviation from unity. Table VII lists the fitted results for the $\overline{D}^0/D^0$ ratio from various centralities. In the most central collisions, $\overline{D}^0$ yield is higher than the D^0 yield by $\sim 4.9\sigma$ on average. This can potentially be explained by the finite baryon density of the system at RHIC, from which we expect the Λ_c^-/Λ_c^+ ratio to be smaller than unity [47]. The total charm quark and anti-charm quark should be conserved since they are created in pairs, which results in larger $\overline{D}^0$ yield than the D^0. This calls for the precise
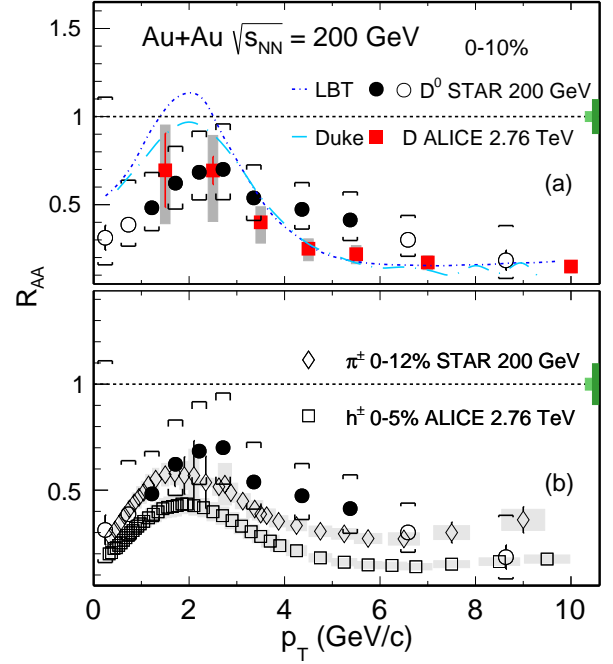

FIG. 32. D^0 R_{AA} in most central (0-10%) Au+Au collisions at $\sqrt{s_{NN}} = 200\,\text{GeV}$, comparison to ALICE D meson result in most central (0-10%) Pb + Pb collisions at $\sqrt{s_{NN}} = 2.76\,\text{TeV}$, and hadron from ALICE and $\pi^{\pm}$ from STAR. Also compared to model calculations from LBT and Duke group [41–43]. The statistical and systematic uncertainties are similar as in previous plots.
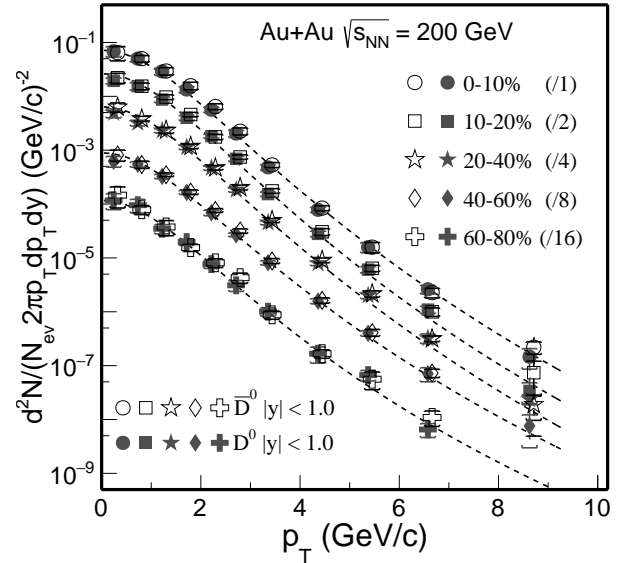

FIG. 33. D^0 and $\overline{D}^0$ invariant yield at mid-rapidity ($|y| < 1$) vs. transverse momentum for different centrality classes. Error bars (not visible for many data points) indicate statistical uncertainties and brackets depict systematic uncertainties. Global systematic uncertainties in $B.R.$ and N_{bin} are not plotted. Solid lines depict Levy function fits.
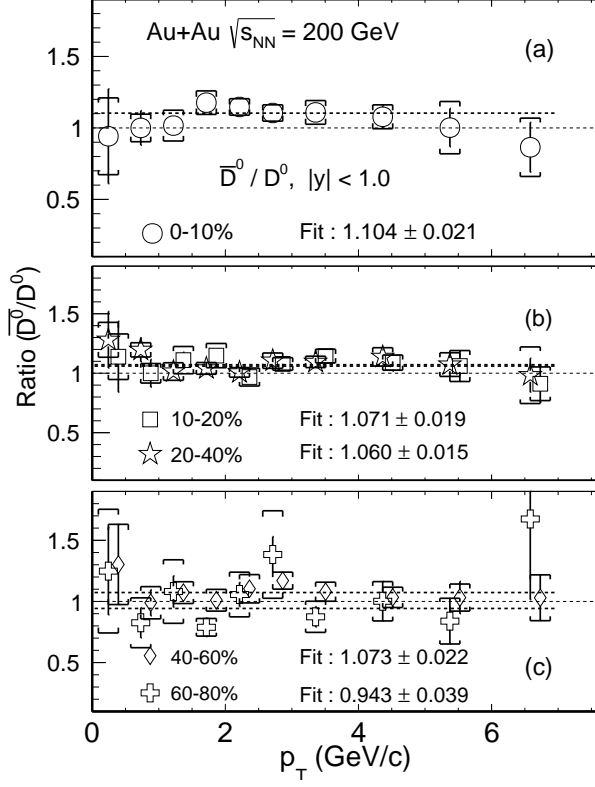
FIG. 34. $\overline{D}^0/D^0$ invariant yield ratio at mid-rapidity ($|y| < 1$) vs. transverse momentum for different centrality classes. Error bars indicate statistical uncertainties and brackets depict systematic uncertainties. Dashed lines depict a constant function fits.

TABLE VII. $\overline{D}^0/D^0$ ratio for various centrality bins obtained from the fit to data distributions in Fig. 34.

Centrality	$\overline{D}^0/D^0$
0–10 %	1.104 ± 0.021
10–20 %	1.071 ± 0.019
20–40 %	1.060 ± 0.015
40–60 %	1.073 ± 0.022
60–80 %	0.943 ± 0.039
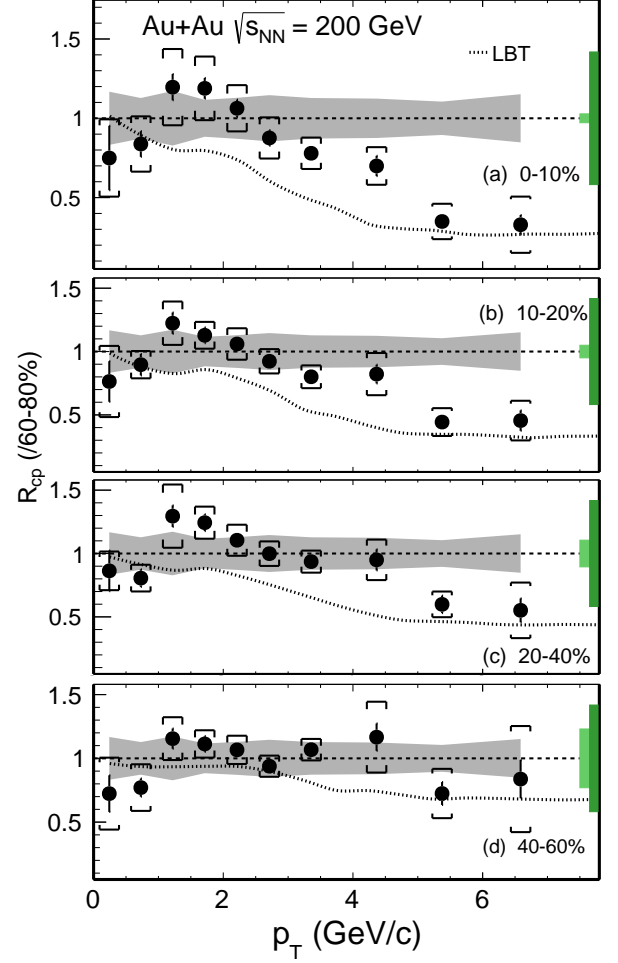
FIG. 35. D^0 R_{CP} with the 60–80% spectrum as the reference for different centrality classes compared to model calculations shown by dashed lines [41, 42]. The statistical and systematic uncertainties are shown as error bars and brackets on the data points. The grey bands around unity depict the systematic uncertainty due to vertex resolution correction, mostly from the 60–80% reference spectrum. The light and dark green boxes on the right depict the normalization uncertainty in determining the N_{bin}.

measurement of D^+/D^- and D_s^+/D_s^- in the future.

E. Comparison to Models

Over the past several years, there have been rapid developments in the theoretical calculations on the charm hadron production. Here we compare our measurements to several recent calculations based on the Duke model and the Linearized Boltzmann Transport (LBT) model.

The Duke model [43, 48] uses a Langevin stochastic simulation to trace the charm quark propagation inside the QGP medium. Both collisional and radia-

tive energy losses are included in the calculation and charm quarks are hadronized via a hybrid approach combining both coalescence and fragmentation mechanisms. The bulk medium is simulated using a viscous hydrodynamic evolution and a hadronic cascade evolution using the UrQMD model [49]. The charm quark interaction with the medium is characterized using a temperature and momentum-dependent diffusion coefficient. The medium parameters have been constrained via a statistical Bayesian analysis by fitting the previous experimental data of R_{AA} and v_2 of light, strange and charm hadrons [43]. The extracted charm quark spatial diffusion coefficient at zero momentum $2\pi T D_s|_{p=0}$ is about 1–3 near T_c and exhibits a positive slope for its temper-
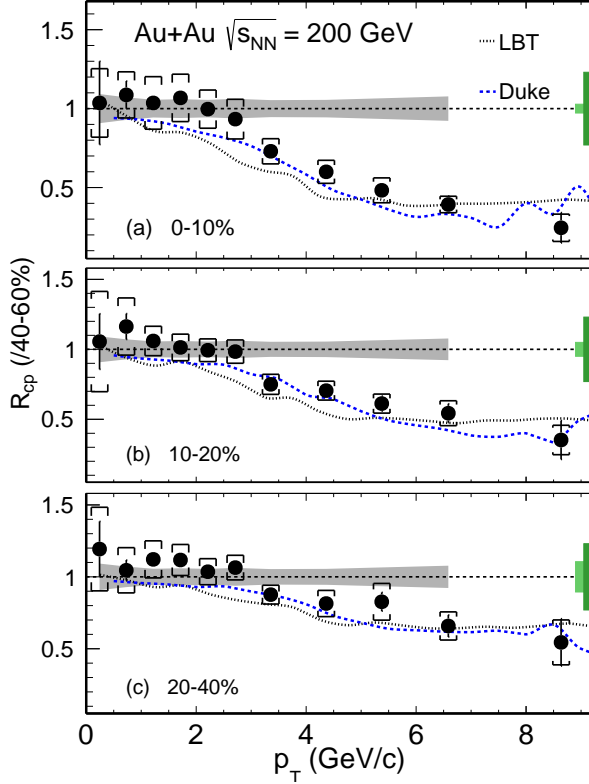
FIG. 36. D^0 R_{CP} with the 40–60% spectrum as the reference for different centrality classes compared to model calculations from LBT (black dashed lines) and Duke (blue dashed lines) groups [41–43]. The statistical and systematic uncertainties are shown as error bars and brackets on the data points. The grey bands around unity depict the systematic uncertainty due to vertex resolution correction, mostly from the 40–60% reference spectrum. The light and dark green boxes on the right depict the normalization uncertainty in determining the N_{bin}.

ature dependence above T_c.

The Linearized Boltzmann Transport (LBT) calculation [41] extends the LBT approach developed before to include both light and heavy flavor parton evolution in the QGP medium. The transport calculation includes all $2 \rightarrow 2$ elastic scattering processes for collisional energy loss and the higher-twist formalism for medium induced radiative energy loss. It uses the same hybrid approach as in the Duke model for charm quark hadronization. The heavy quark transport is coupled with a 3D viscous hydrodynamic evolution which is tuned for light flavor hadron data. The charm quark spatial diffusion coefficient is estimated via the $2\pi T D_s = 8\pi/\hat{q}$ ($\hat{q}$, is the quark transport coefficient due to elastic scatterings) at parton momentum $p = 10 \, \text{GeV}/c$. The $2\pi T D_s$ is ~3 at T_c and increases to ~6 at $T = 500 \, \text{MeV}$ [42].

Figures 35 and 36 show the measured D^0 R_{CP} compared to the Duke and LBT model calculations with the 60–80% and 40–60% reference spectra respectively. The

R_{CP} curves from these models are calculated based on the D^0 spectra provided by each group [41–43]. The Duke model did not calculate the spectra in the 60–80% centrality bin due to the limitation of the viscous hydrodynamic implementation. In Fig. 32 for the most central collisions, there are also calculations for the D^0 R_{AA} from the Duke and LBT group, respectively. These two models also have the prediction for the D^0 v_2 measurements for Au+Au collisions at $\sqrt{s_{NN}} = 200 \, \text{GeV}$ [16]. Both model calculations match our new measured R_{CP} data well. However, the much improved precision of these new measurements are expected to further constrain the theoretical model uncertainties in these calculations.

VII. CONCLUSIONS

In summary, we report the improved measurement of D^0 production yield in Au+Au collisions at $\sqrt{s_{NN}} = 200 \, \text{GeV}$ with the STAR HFT detector. D^0 invariant yields are presented as a function of p_T in various centrality classes. There is a hint (1.5 σ) that the p_T integrated D^0 yields at mid-rapidity in mid-central and central Au+Au collisions are smaller than that measured in $p+p$ collisions, indicating that CNM effects and/or hadronization through quark coalescence may play an important role in Au+Au collisions. This calls for precise measurements of D^0 production in p/d+A collisions to understand the CNM effects as well as other charm hadron states in heavy-ion collisions to better constrain the total charm quark yield.

The $\overline{D}^0$ yield is observed to be higher than the D^0 in the most central collisions, by ~4.9σ on average. This is potentially consistent with the picture of the finite baryon density of the system at RHIC, from which we expect the Λ_c^-/Λ_c^+ ratio to be smaller than unity and results in larger $\overline{D}^0$ yield than the D^0.

The D^0 spectra at low p_T and low m_T are fit to the exponential function and the Blast-Wave model to study the radial collectivity. The slope parameter extracted from the exponential function fit for D^0 mesons follows the same linearly increasing trend vs. particle mass as ϕ, Λ, Ξ^-, Ω^- particles, but different from the trend of π, K, p particles. The extracted kinetic freeze-out temperature and transverse velocity from the Blast-Wave model fit are comparable to the fit results of ϕ, Ξ^- multi-strange-quark hadrons, but different from those of π, K, p. These suggest that D^0 hadrons show a radial collective behavior with the medium, but freeze out from the system earlier and gain less radial collectivity compared to π, K, p particles. This observation is consistent with collective behavior observed in v_2 measurements. The fit results also suggest that D^0 mesons have similar kinetic freeze-out properties as multi-strange-quark hadrons ϕ, Ξ^-.

The nuclear modification factors R_{CP} of D^0 mesons are presented with both 60–80% and 40–60% centrality spectra as the reference, respectively. The D^0 R_{CP} is sig-

nificantly suppressed at high p_T and the suppression level is comparable to that of light hadrons at $p_T > 5\,\text{GeV/c}$, re-affirming our previous observation [12]. This indicates that charm quarks lose significant energy when traversing through the hot QCD medium. The D^0 R_{CP} is above the light hadron R_{CP} at low p_T. We compare our D^0 R_{CP} measurements to two recent theoretical model calculations from LBT and Duke group. These two models have the $2\pi T D_s$ value around 1-3 near T_c and agree with our new R_{CP} measurements. We expect the new data points with much improved precision can be used in the future to further constrain our understanding of the charm-medium interactions as well as to better determine the medium transport parameter.

VIII. ACKNOWLEDGEMENT

[1] J. Adams *et al.* (STAR), Nucl. Phys. **A757**, 102 (2005).
[2] K. Adcox *et al.* (PHENIX), Nucl. Phys. **A757**, 184 (2005).
[3] B. Muller, J. Schukraft, and B. Wyslouch, Ann. Rev. Nucl. Part. Sci. **62**, 361 (2012).
[4] L. Adamczyk *et al.* (STAR), Phys. Rev. Lett. **116**, 062301 (2016).
[5] B. B. Abelev *et al.* (ALICE), JHEP **06**, 190 (2015).
[6] Z. Lin and M. Gyulassy, Phys. Rev. C **51**, 2177 (1995).
[7] M. Cacciari, P. Nason, and R. Vogt, Phys. Rev. Lett. **95**, 122001 (2005).
[8] G. D. Moore and D. Teaney, Phys. Rev. C **71**, 064904 (2005).
[9] B. Abelev *et al.* (ALICE), JHEP **09**, 112 (2012).
[10] J. Adam *et al.* (ALICE), JHEP **03**, 081 (2016).
[11] A. M. Sirunyan *et al.* (CMS), Physics Letters B **782**, 474 (2018).
[12] L. Adamczyk *et al.* (STAR), Phys. Rev. Lett. **113**, 142301 (2014), erratum: arXiv:1809.08737 [nucl-ex].
[13] B. Abelev *et al.* (ALICE), Phys. Rev. Lett. **111**, 102301 (2013).
[14] B. Abelev *et al.* (ALICE), Phys. Rev. C **90**, 034904 (2014).
[15] A. M. Sirunyan *et al.* (CMS), Phys. Rev. Lett. **120**, 202301 (2018).
[16] L. Adamczyk *et al.* (STAR), Phys. Rev. Lett. **118**, 212301 (2017).
[17] H. Qiu (STAR), Nucl. Phys. **A931**, 1141 (2014).
[18] M. Anderson *et al.*, Nucl. Instrum. Meth. **A499**, 659 (2003).
[19] W. J. Llope (STAR), Nucl. Instrum. Meth. **A661**, S110 (2012).
[20] L. Adamczyk *et al.* (STAR), Phys. Rev. D **86**, 072013 (2012).
[21] W. J. Llope *et al.*, Nucl. Instrum. Meth. **A522**, 252 (2004).
[22] G. Contin *et al.*, Nucl. Instrum. Meth. A **907**, 60 (2018).
[23] A. Hoecker *et al.*, (2007), arXiv:0703039 [physics].
[24] M. Tanabashi *et al.* (Particle Data Group), Phys. Rev. D **98**, 030001 (2018).
[25] S. Agostinelli *et al.*, Nucl. Instrum. Meth. A **506**, 250 (2003).
[26] M. Gyulassy and X.-N. Wang, Computer Physics Communications **83**, 307 (1994).
[27] J. Adams *et al.* (STAR), Phys. Rev. Lett. **92**, 112301 (2004).
[28] M. Shao *et al.*, Nucl. Instrum. Meth. **A558**, 419 (2006).
[29] Y. Xu *et al.*, Nucl. Instrum. Meth. **A614**, 28 (2010).
[30] V. Greco, C. Ko, and R. Rapp, Physics Letters B **595**, 202 (2004).
[31] Y. Oh *et al.*, Physical Review C - Nuclear Physics **79**, 1 (2009).
[32] M. He, R. J. Fries, and R. Rapp, Phys. Rev. Lett. **110**, 112301 (2013).
[33] M. Kaneta, *Thermal and Chemical Freeze-out in Heavy Ion Collisions*, Ph.D. thesis, Hiroshima U. (1999).
[34] T. Csorgo and B. Lorstad, Phys. Rev. C **54**, 1390 (1996).
[35] P. F. Kolb and U. W. Heinz, Quark Gluon Plasma 3 , 634 (2003).
[36] E. Schnedermann *et al.*, Phys. Rev. **C48**, 2462 (1993).
[37] Z. Tang *et al.*, Phys. Rev. C **79**, 051901 (2009).
[38] B. I. Abelev *et al.* (STAR), Phys. Rev. Lett. **97**, 152301 (2006).
[39] B. I. Abelev *et al.* (STAR), Phys. Rev. C **79**, 064903 (2009).
[40] G. Agakishiev *et al.* (STAR), Phys. Rev. Lett. **108**, 072301 (2012).
[41] S. Cao *et al.*, Phys. Rev. C **94**, 014909 (2016).
[42] S. Cao, private communication.
[43] Y. Xu *et al.*, Phys. Rev. C **97**, 014907 (2018).
[44] M. Lisovyi, A. Verbytskyi, and O. Zenaiev, The European Physical Journal C **76**, 397 (2016).

[45] B. Abelev *et al.* (ALICE), Physics Letters B **720**, 52 (2013).

[46] A. Adare *et al.* (PHENIX), Phys. Rev. Lett. **101**, 232301 (2008).

[47] A. Andronic *et al.*, Physics Letters B **571**, 36 (2003).

[48] S. S. Cao, G. Qin, and S. A. Bass, Phys. Rev. C **92**, 024907 (2015).

[49] M. Bleicher *et al.*, Journal of Physics G: Nuclear and Particle Physics **25**, 1859 (1999).